Construction and qualification of a micro-tensile testing machine for lower scale digital image correlation applied to Zirconium alloys

A thesis submitted to:

Escola Tècnica Superior d'Enginyeria Industrial de Barcelona

Universitat Politècnica de Catalunya

Performed at:

Laboratory for Nuclear Materials

Nuclear Energy and Safety Research Department

Paul Scherrer Institut, Switzerland

Supervised by:

Dr Ralph Spolenak, Eidgenössische Technische Hochschule Zürich

Dr Javier Dies, Universitat Politècnica de Catalunya

Dr Stéphane Valance, Paul Scherrer Institut

Presented by:

Marc Raventós Tato

Barcelona, June 2014

Abstract

The aim of this project is the construction, programming and operation of a thermo-mechanical testing machine for the study of the mechanical properties of nuclear fuel cladding material. The strain information is estimated using Digital Image Correlation techniques on pictures taken with a digital camera during the thermo-mechanical test. This prototype will provide better understanding of the local effects of thermo-mechanical loads of hydrogenated Zircaloy cladding.

To understand the relevance of this topic, comprehension of how and why the hydrogen uptake process takes place inside Zircaloy claddings is necessary. A short explanation of his process as well as the relation between hydrogen content and the mechanical properties of Zircaloy is the introduction to this work.

The next part of this project is dedicated to the setup of the structure and the installation of the five different electric systems of the prototype: force, heating, vacuum, control and optical system. An explanation of the LabView code designed to control the machine is included in this part.

After this explanation, qualification of the optical system and Digital Image Correlation code is presented later, with thermal essay results. Hydrogenated Zircaloy sample preparation and experimental set-up is detailed for future experiments. The qualification of the machine finishes with the estimation of the linear thermal coefficient of the machine using DIC.

ETSEIB

Table of Contents

List of figures

List of tables

Glossary

PSI: Paul Scherrer Institut

UPC: Universitat Politècnica de Catalunya

ETSEIB: Escola Tècnica Superior d'Enginyeria Industrial de Barcelona

DIC: Digital Image Correlation

PWR: Pressurized Water Reactor

BWR: Boiling Water Reactor

wt%: percentage by weight

NPP: Nuclear Power Plant

ppm: parts per million

hcp: Hexagonal Close Packed

fct: Face Centred Tetragonal

fcc: Face Centred Cubic

vi: virtual instrument

TSSD: Terminal Solid Solubility of Dissolution

TSSP: Terminal Solid Solubility of Precipitation

Zr-2: Zircaloy-2

Zr-4: Zircaloy-4

DAQ: Data AQuisition

SS: Subset Size

SZ: Search Zone

Preface

The current generation of reactors is an evolutionary variant of light water reactor, and most part of the technology involved is mature. This type of reactor is going to be dominant in the energetic panorama at least until the 4th generation enters the market. Thereby the study of materials and techniques used today is still of great interest.

The nuclear industry struggles to reach high burnup rates during operation cycles. The reasons are obvious from an economical point of view, but these technical challenges require a better understanding of the materials behaviour. Cladding material is a key material nowadays; it is the first barrier preventing release of radioactive material. Therefore the study of its mechanical behaviour at high burnup is essential to use the nuclear technology safely.

Zircaloy is the commercial trade name of specific zirconium alloys used to manufacture cladding material for nuclear fuel rods since decades. Due to its low cross-section in the neutronic thermal spectrum, high hardness, ductility and corrosion resistance, zirconium is a material of choice for cladding tubes manufacturing.

During reactor operation, the cladding material finds itself constantly in contact with water at high temperatures. One of the phenomena that takes place is the diffusion of H+ ions inside of the Zircaloy. Depending on temperature and concentration, hydrogen can be found in the cladding either in solid solution, hydrides or both. Metallic hydrides have a lower density and higher brittleness than the original alloy, and their precipitation rises dramatically as the material cools down to normal temperatures. However, presence of hydrogen in solid solution or hydrides induces local effects on the displacement field that cannot be investigated usual macroscopic approaches.

It is required a technique that permits the determination of changes in the surface displacement field and field measurement from previously taken images, while applying a thermo-mechanical load. The technique used in this project is Digital Image Correlation.

1 Introduction

Whereas equipment exists for the investigation of mechanical and material properties at large scale – tensile testing machines – and at low to very low scale – in situ SEM, etc. –, there is a lack of experimental approaches in mesoscopic scale, where a media can still be considered to be a continuum, but where local effects can take place and are to be resolved. With the rise of Digital Image Correlation (DIC), it is possible to foresee an experimental approach in these intermediate scales. The displacement field in a thermo-mechanically stressed media, a primary field in mechanics, can be measured locally up to a resolution of micrometers.

We would like to apply such an approach to various studies on zirconium alloys. Acquisition of pictures of a sample surface is however not enough: it should also be possible to apply a thermo-mechanical loading on the sample, and to ensure a stable observation. It is therefore required to design a specifically dedicated thermo-mechanical testing machine which would enable us to retrieve local deformation in a zirconium alloy sample submitted to a thermo-mechanical loading.

1.1 Zircaloy and hydrogen uptake

During the operation of the reactor, oxidation of Zircaloy takes place in the external surface of the cladding material. Thereby, hydrogen is released into the reactor. Part of this hydrogen diffuses back through the oxide layer to the inner part of the cladding. Other sources of hydrogen like water chemistry or electrolysis are negligible. [1]

The hydrogen concentration inside the cladding is not homogenous. Hydrogen diffuses inside the zirconium matrix through vacancies and interstitial defects, driven by concentration, temperature and stress gradients.

Let us take cladding during operation at 315° (outer surface) with a specific concentration of hydrogen dissolved inside of the cladding. During reactor cooldown, the outer part of the cladding will lower its temperature faster than the inner part. Hydrogen starts to precipitate earlier in the outer region thus the amount of hydrogen remaining in solid solution decreases. The dissolved hydrogen concentration gradient grows between the inner and the outer part of the cladding and the diffusion effect displaces more hydrogen to inner layer. As the cooldown process is so slow, hydrogen "has time enough" to reach equilibrium conditions at concentration for every temperature. Figure 1.1 shows an example of hydrides precipitate inside the cladding.

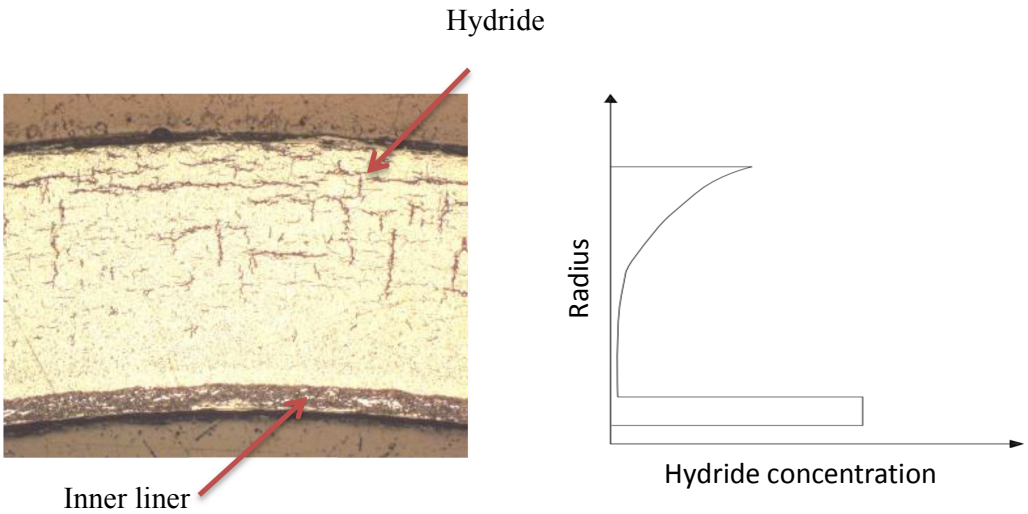

Figure 1.1: Operated Zircaloy cladding cross-section with visible δ-Hydride platelets. Qualitative diagram of the hydride distribution inside the cladding.

The next tables show standard information of cladding dimensions, composition and hydrogen uptake for BWR and PWR reactors and different burn-ups.

Outer Diameter [mm]	Thickness [mm]	Length [mm]
9.5	0.6	$4x10^3$

Table 1.1: Standard cladding dimensions

	Reactor Type	Zr	Sn	Fe	Cr	Ni
Zircaloy-2	BWR	98.250%	1.45%	0.135%	0.100%	0.055%
Zircaloy-4	PWR	98.23%	1.45%	0.210%	0.1%	-

Table 1.2: Most usual Zircaloy composition (wt%).

	Low burn-up 20 to 40 MWd/kgU	High burn-up 50 to 75 MWd/kgU
BWR (285 °C)	20 to 100 ppm	100 to 500 ppm
PWR (315 °C)	20 to 200 ppm	100 to 1000 ppm

Table 1.3: Hydrogen uptake relative to the burnup.

1.2 Hydrogen in zirconium alloys

Hydrogen and zirconium form several different compounds in a close range of concentrations. α-Zr is the most stable phase at room temperature. It follows a hexagonal closed-pack structure and can dissolve only a limited amount of hydrogen, up to 0.069% of hydrogen at 550°C. β-Zr forms at 863°C with no hydrogen content, and has a eutectoid point at 0.55% of hydrogen and 550°. This is a body-centered cubic structure and can dissolve more than 1.2% of hydrogen at 900°C. This β-zirconium suffers a eutectoid transformation when cooled below 550°C, creating a mixture between α-Zr and δ-Zr, which precipitate into the zirconium matrix. δ-Hydrides are a face-centered cubic stable phase of zirconium between 1.5 and 1.66 weight percentage for a large range of temperatures. ε-Zr is the hydride face-center tetragonal phase formed between 1.66 and 2% of hydrogen. The Figure 1.2 shows the phase diagram of hydrogen and zirconium[2].

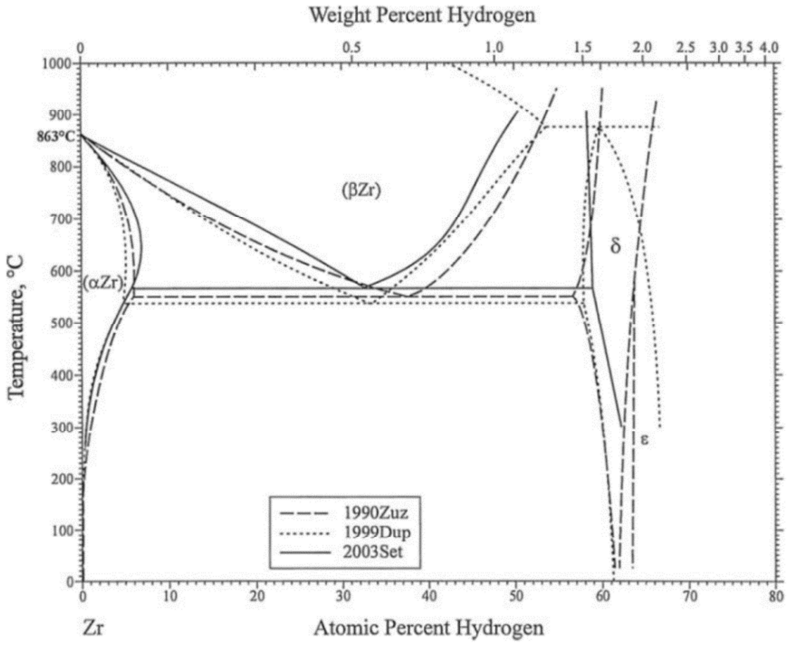

Figure 1.2: H-Zr Phase diagram[2].

Hydrogen has low solubility in zirconium under 600°C, this property causes the apparition of precipitates in the form of delta-hydrides under this temperature. α-Zr and δ-Zr are the only relevant Zr-H mixtures during operation of the reactor, but it does not apply for out-of-normal operation situation involving a fast cooldown. Only the mechanical effects of δ-Hydrides are of interest in this work.

Our main region of interest for zirconium simplifies the phase diagram to Figure 1.3:

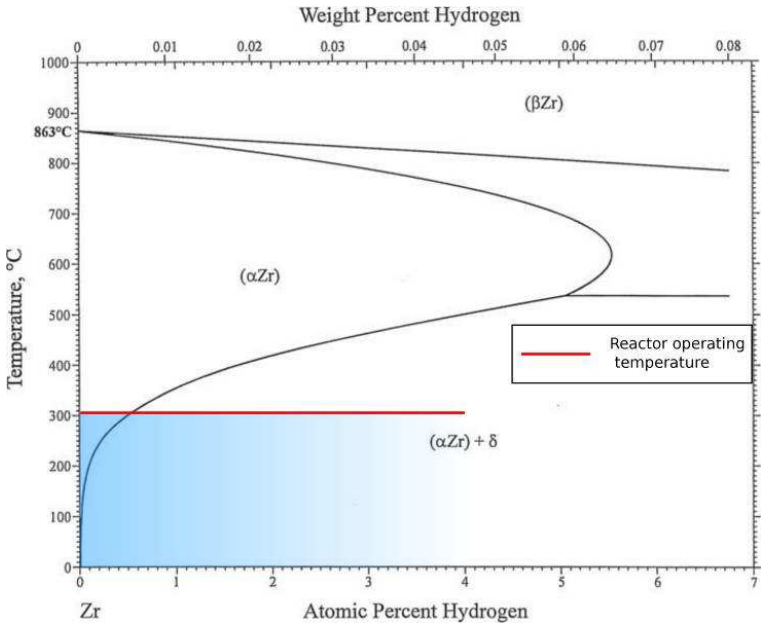

Figure 1.3: H-Zr Magnified phase diagram for a NPP during normal operation.

In a first look to Table 1.4, one can be observe that the lower density of δ-hydrides relative to α-Zr implies a local volume change in the material. The conservation of material continuity is then assured by the buildup of local stress.

Phase	Structure	Lattice constants [nm]		Density	Mean interatomic distance
		a	c	[g/cm3]	[nm]
α-Zr	hcp	0,323	0,515	6,51	0,322
γ-(ZrH)	fct	0,46	0,497	5,82	0,334
δ-(ZrH1,6)	fcc	0,478	-	5,64	0,338
ε-(ZrH2)	fct	0,498	0,445	5,61	0,339

Table 1.4: Crystallographic properties of the different phases[3].

1.1.1. Terminal Solid Solubility curves

The dissolution and precipitation phenomena of hydrogen in zirconium are effectively explained through the curves of Terminal Solid Solubility (TSS) in Figure 1.4.

The TSSD curve shows the temperature required during heating to dissolve all the hydrogen at a certain concentration. The TSSP shows the temperature required during cooling which will make all the hydrogen precipitate at every concentration.

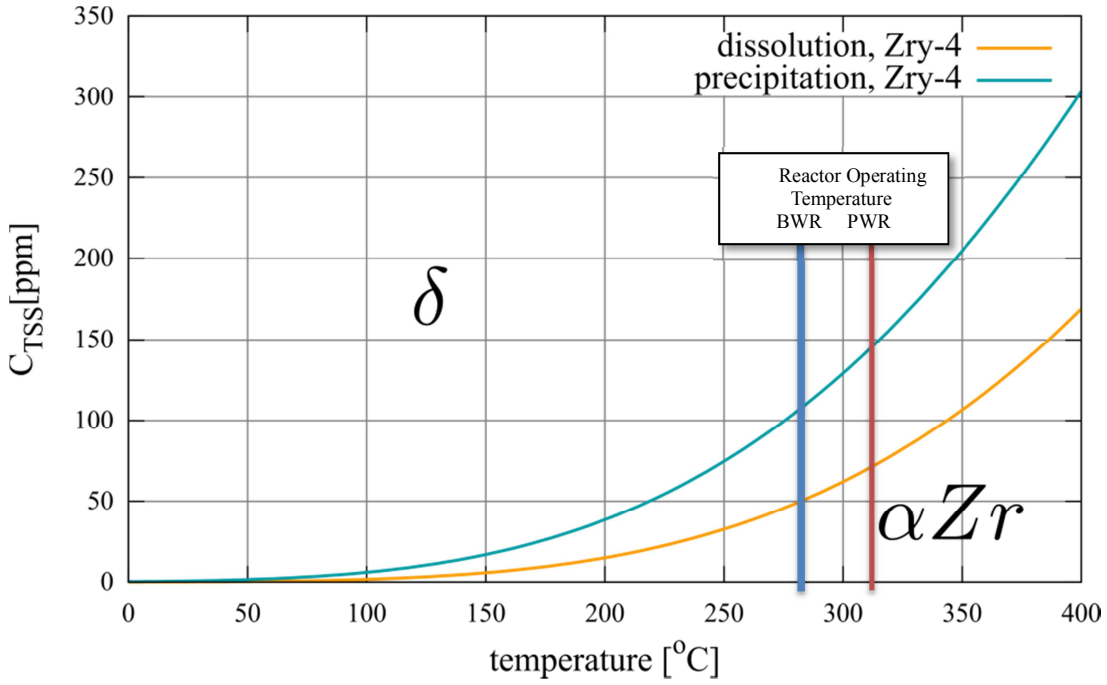

Figure 1.4: Terminal solid solubility curves of hydrogen in zirconium.

This difference between the curves of precipitation and dissolution has often been referred as “hysteresis” of dissolution[4]. The hysteresis is explained following Figure 1.5.

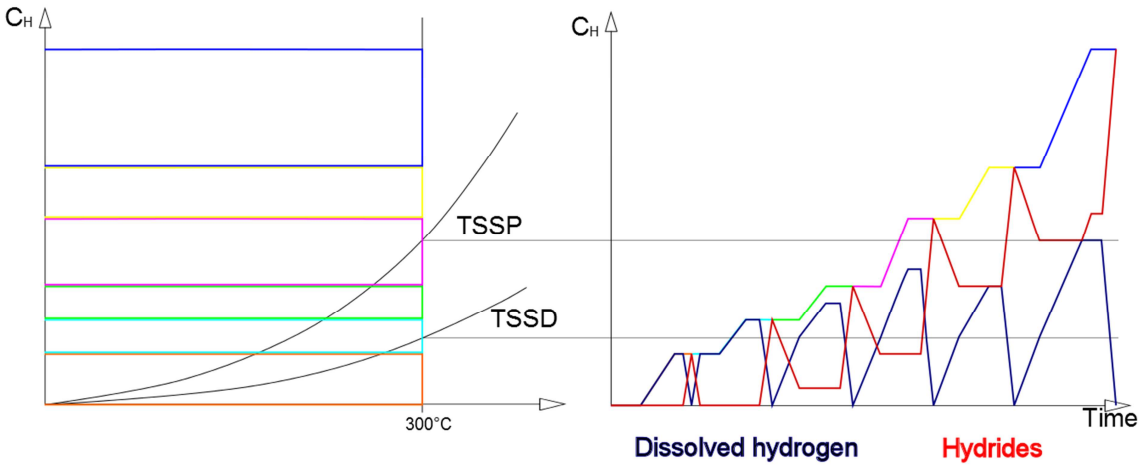

Figure 1.5: Example of hydrogen uptake during several cycles of irradiation.

During the first cycle (orange), all the hydrogen dissolves in the zirconium. At the end of this first cycle the cladding is cooled down, the solubility drops and all the hydrogen precipitates as hydrides.

During the second cycle (light blue), hydrogen dissolves back again in the cladding when the temperature rises and the new hydrogen taken up is dissolved as well. Notice that at the end of the second cycle the concentration of hydrogen inside the cladding is higher than the value of TSSD for operation temperature. For this reason not all the hydrogen can be dissolved in the cladding at the beginning of the third cycle. However the cladding still admits hydrogen dissolved, so the new hydrogen taken up during the third reactor cycle will appear in solid solution inside the Zircaloy.

This process repeats in every cycle until the last one (dark blue). In the last cycle, the concentration of dissolved hydrogen reaches the terminal solid solubility of precipitation, no more hydrogen can dissolve in the cladding, and therefore the rest of it precipitates. This process would repeat every cycle in the future for higher hydrogen contents.

1.2.1 Hydrogen in solid solution αZr

Figure 1.6 and *Figure 1.7* show the evolution of elastic properties of hydrogenated Zircaloy depending on the hydrogen content and temperature[5].

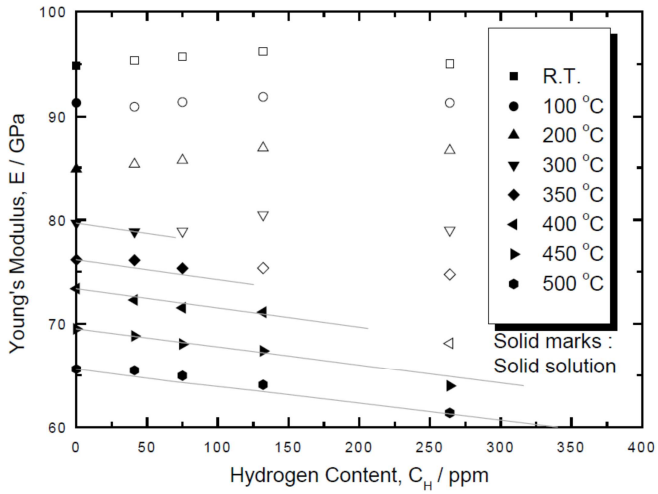

Figure 1.6: Young modulus for hydrogen in solid solution (black dots)

From the least-square method, the next equation is determined for the young modulus ratio.

$$\frac{E}{E_0} = 1 - 2.518x10^{-4}xC_H$$

Young modulus drops linearly with hydrogen content in solid solution.

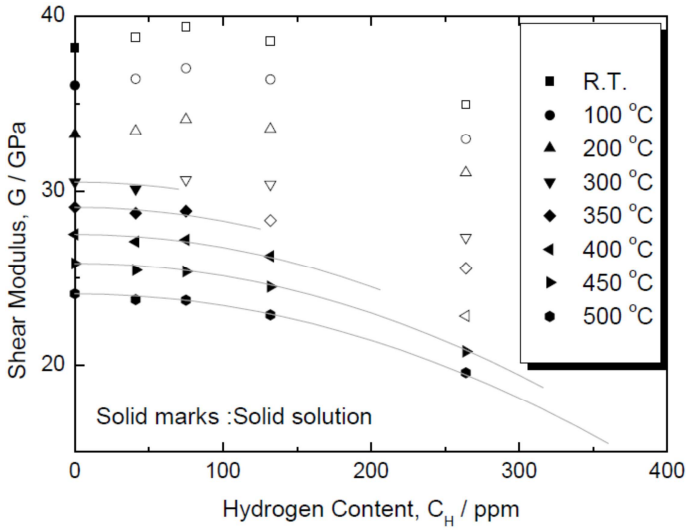

Figure 1.7: Shear modulus for hydrogen in solid solution (black dots)

$$\frac{G}{G_0} = 1 - 2.747x10^{-6}xC_H^2$$

The shear modulus drops parabolically with the hydrogen content, as shown in the previous equation.

Considering 70 ppm of hydrogen in solid solution during operation for a low burnup fuel, the fraction of the initial modulus value remaining would be:

$$\frac{E}{E_0} = 0.982374 \qquad \frac{G}{G_0} = 0.986540$$

Considering 140 ppm of hydrogen in solid solution during operation for a high burnup fuel, the fraction of the initial modulus value remaining would be:

$$\frac{E}{E_0} = 0.964748 \qquad \frac{G}{G_0} = 0.9461588$$

The impact of hydrogen in solid solution on the mechanical behaviour of Zircaloy reduces slightly the stiffness of the material.

This data is relevant for the hcp α-Zr phase during operation under normal conditions. β-Zr can only be formed over 550°C, that is to say, only in PWR or BWR reactors under accidental conditions.

1.2.2 Zirconium δ-hydrides

δ-hydrides are the only precipitate of hydrogen formed during operation and cooldown inside the reactor. During operation, the hydrogen inside the cladding is diffused due to the temperature gradient from the inner cladding radially to the outside. This provokes high concentration of hydrides towards the external part of the cladding.

1.2.2.1 Embrittlement

The embrittlement is a change in the mechanical properties of the cladding due to hydrogen pick-up. It is especially significant in the temperature range between 100 and 315 °C, which is the normal operation range of temperatures. At higher temperatures, the solubility of hydrogen in Zircaloy increases and the embrittlement decreases significantly. [5]

1.2.2.2 Delayed hydride cracking

Hydrides appear mainly in the form of platelets in the outer part of the cladding, due to the diffusion effect. The presence of incipient cracks acts as stress raisers in the cladding tubes and favors the orientation of the hydrides in the tubes radial direction (radial hydrides).[4]

As a hydride grows in front of a crack and reaches certain length, it cannot support the local stresses further and will undergo a brittle fracture, as can be seen in Figure 1.8. The crack then advances by a distance approximately equal to the length of the hydride and arrests in the matrix. This process then repeats itself.

The cladding tube manufacturing procedure is optimize to favor hydrides precipitation in a "less harmful direction" as possible, to say, circumferential direction. In this direction, the hydride platelets are tangent to the hoop component of the stress field which is the most critical with respect to cladding integrity. [6]

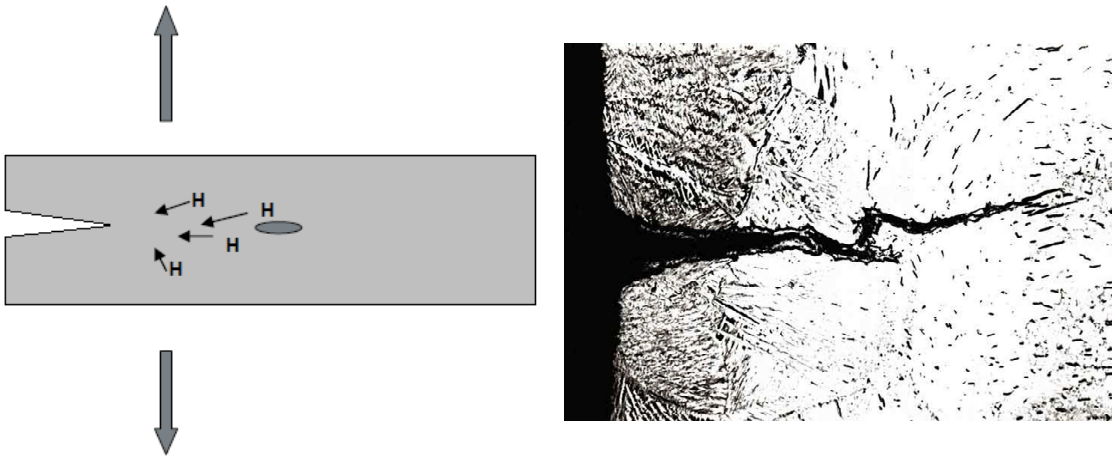

Figure 1.8: Migration of hydrogen atoms from the platelet to the crack tip.

1.2.2.3 Blistering

Under conditions where oxide spallation occurs, the cladding wall is penetrated by the coolant and lens shaped hydrides may form in the inside. These are called Blisters.

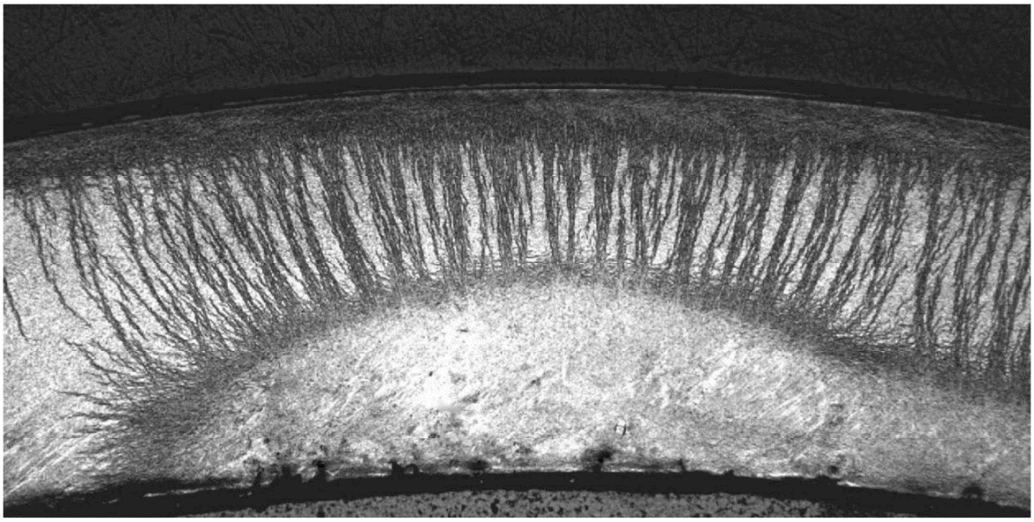

Figure 1.9: Hydride blister inside a cladding tube.

They form a highly brittle zone inside the Zircaloy which increases greatly the chance of brittle fracture. Once the blister is formed, hydrogen migrates from the blister to the outer layer of the cladding in the radial direction, as can be seen in both Figure 1.9 and Figure 1.10.

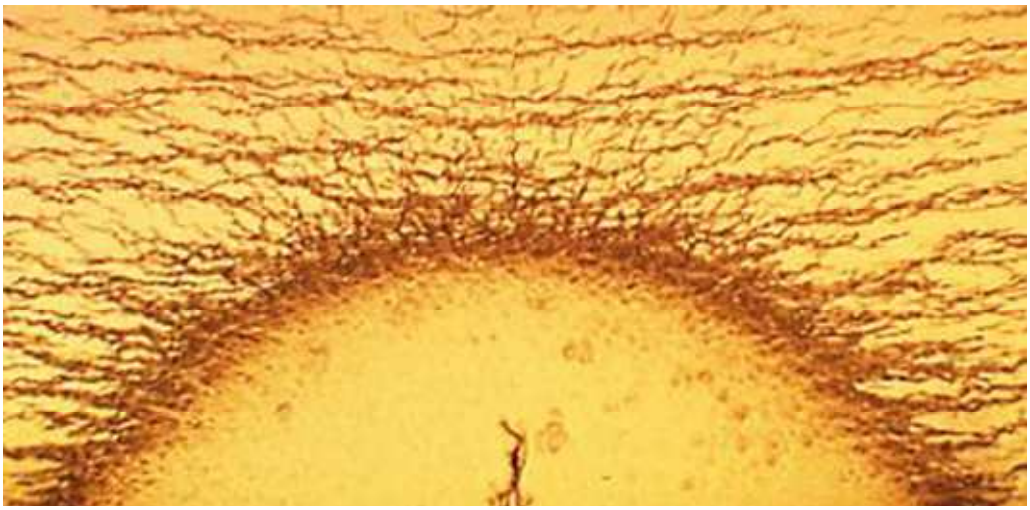

Figure 1.10: Hydride blister in Zircaloy with beginning of crack.

2 Machine requirements

The system is primarily targeted to the test of Zircaloy in sheet form with a usual thickness of 0.6 mm. The width of the sample, depending on the foreseen tests, will evolve between 0.6 and 3 mm. In a first approach, the ratio of the gauge length to the square root of the specimen cross section area should lie between 5 and 10. This gives us a gauge length comprised between 3.0 and 13.4 mm.

The uni-axial tensile tests will cover the elastic domains; plastic domains could be covered with a smaller cross section.

2.1 Functional elements

Without any *a-priori* view on the machine to be designed, it is possible to split the overall system as a function of the objective to be fulfilled:

- A tensile testing machine, itself partitioned in a structural frame and an actuator
- A cell able to hold low to high vacuum
- A sample heating system
- A loading, temperature, force and displacement, control and monitoring system
- A vacuum 'production' machine
- An image acquisition system, partitioned in a structural positioning frame and optic/video system

From previous experience, some technological aspects are *a-priori* requested:

- Inside vacuum cell tensile testing machine structure
- Outside vacuum cell tensile testing machine actuator
- Telecentric lens for the optical system

3 Pieces and construction

The aim of this chapter is to detail the process of construction and programming of the machine to anyone who is interested in replicating or designing a machine for the same purpose. Said so, the content here should be understood as a construction guide as well as an academic document.

3.1 Frame

The frame is a structure made of aluminum profiles from Rose+Krieger. It gives a place for the machine to rest and provides stability and sturdiness.

80x40mm cross section		40x40mm cross section	
Piece	**Quantity**	**Piece**	**Quantity**
800mm profile	2	720mm profile	5
720mm profile	4	520mm profile	4
250mm profile	3	480mm profile	2
Corners	16	220mm profile	1
Clamping bracket kits	2	Corners	42
Cover cap	4	Clamping bracket kits	44
M8 mounting kit	64	Adjustable foot	4
		M6 mounting kit	130

Table 3.1: Rose+Krieger piece list.

The guiding linear unit EP60 is the only frame piece and manufactured by Rose+Krieger. It permits the vertical displacement of the piezoelectric actuator and the lower structure. It is attached to the profiles through the EP60 plates.

3.1.1 Frame set up

The construction of the frame took three weeks, taking in account several delays due to wrong piece orders and, partial disassembly of the machine. Also the middle reinforcement parts were thought and suggested to be installed afterwards.

The most common mistake during the mounting process was the absentmindedness regarding all the screw mounting kits. They had to be placed in the profile rails before mounting every clamping bracket kit, and one has to proceed very carefully not to forget every screw.

The first part to be mounted was the top structure. There was a mistake in the piece order and clamping bracket kit S-80 were ordered to fix 80x40 profiles one to each other. Two clamping bracket kits S-40 are needed for every joint. The clamping kits can only be placed in parallel position so there is no chance of mistake.

- It is convenient to use a clamp afterwards to set the clamping bracket kits slightly closer, so that they can be easily fixed to the next profile.

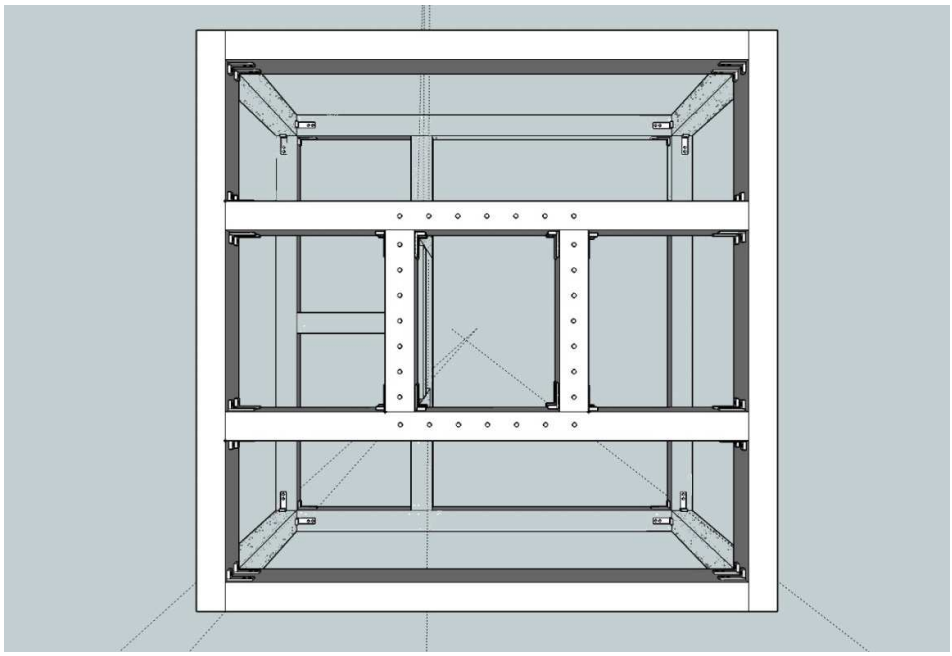

Figure 3.1: 3D Top view of the model of the frame with SketchUp.

The elements that must not be forgotten to place in the central pieces of the structure are:

- 28x M6 screw mounting kits spread 7 in each profile surrounding the center. They will fix the frame plate to the aluminum frame. Can be seen in Figure 3.4.
- 2x S-40 clamping bracket kits on the opposite side of the 720mm pieces for the joint with the central reinforcement.

Observations:

- Notice that the corners are not necessary until the end of the setup. It is much easier to disassembly the machine in case changes have to be made. For every S-80 corner up to 12 screw mounting kits can be used, but 8 of them are enough to keep the joint well fixed.

- All 80x40 profiles have been used until now except for one of the 250mm long.

After the top structure, the second main part is the bottom structure. It is important to set the horizontal profiles as low as possible to the legs of the structure. Therefore, I recommend removing two small plastic pieces attached to the feet of the structure. More specifically, these little pieces would be guided inside the rails of the profile once the feet are set up, as shown Figure 3.2.

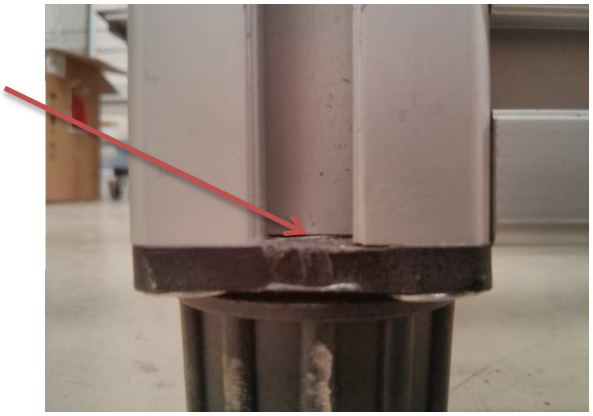

Figure 3.2: Detail of the leg.

Figure 3.3: EP60 installed.

- Before closing the bottom square, the central reinforcement bottom T has to be placed. Do not forget to place the required clamping bracket nut in the horizontal pieces.

In Figure 3.3 the reinforcement is shown as it is built finally. The last 80x40 250mm profile is placed, between the two vertical 40x40 480mm profiles. It is there that the S-80 clamping bracket kits are placed.

- Before attaching the last 80x40 profile make sure that the distance between it and the other 250mm profile is the same as the distance between the fixing surfaces of the guiding linear unit EP60. Anyhow, it is better not to screw the S-80 clamping bracket kits to tight now, so that

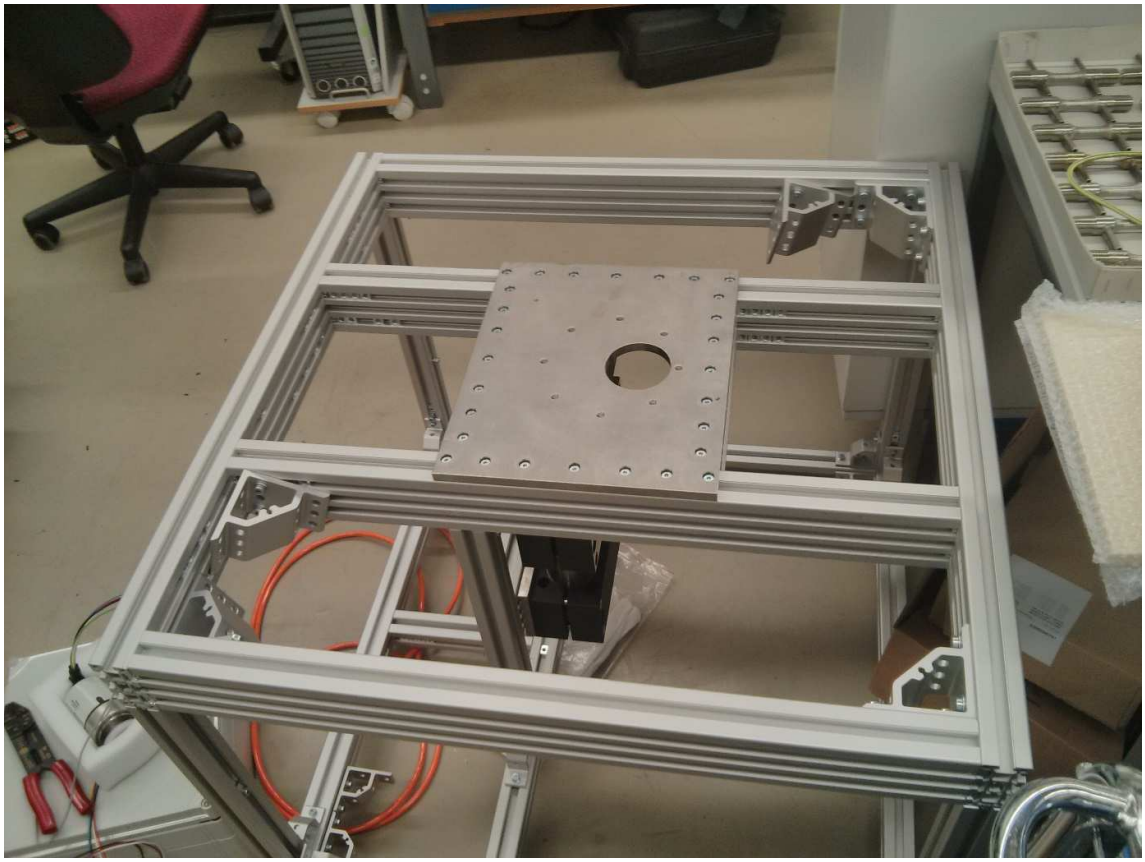

Figure 3.4: Frame with the frame plate, the EP60 plate and the corners.

3.2 Modified and manufactured pieces

Figure 3.5 is a side view of the main parts of the machine assembled. The drafts of the modified or manufactured pieces are included in the ANNEX B.

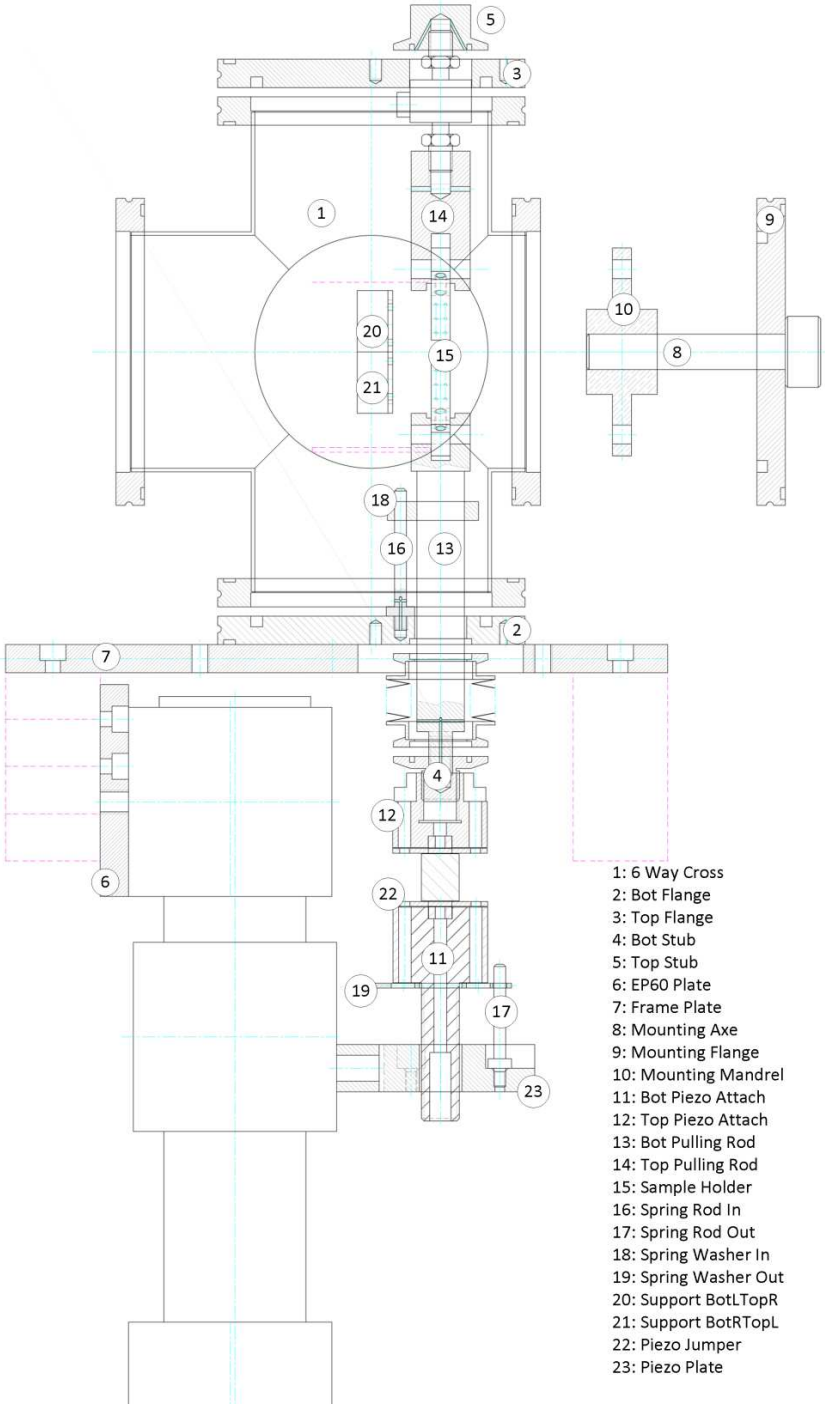

Figure 3.5: Assembly draft of the modified or manufactured pieces.

1) The **6 Way Cross** is the biggest piece of the tensile structure, also called in this document as vacuum chamber or vacuum cell. It contains the vacuum-working pieces that apply the tensile effort, the sample, the infrared radiators, the thermocouples and the force sensor. It is essentially a modified Hositrad ISO-K 100 6 Way Cross. One of the six flanges has been reduced to be used properly with a window for the DIC camera.
2) The **Bottom Flange** is a Hositrad ISO-K 100 blank flange modified with a hole for the bottom pulling rod which permits the movement through it. It has also four threaded holes in the outer part to attach the bellow and three threaded holes in the outer part for the inner spring rods.
3) The **Top Flange** is a Hositrad ISO-K 100 blank flange modified with a hole for the force gauge and four threaded holes in the outer part to attach the top stub.
4) The **Bottom Stub** is a Hositrad blank stub modified with a threaded hole to attach the bottom pulling rod and a thread to attach the top piezo attach. This piece is also fixed vacuum-tight to the bottom flange.
5) The **Top Stub** is a Hositrad blank stub modified with a threaded hole to attach the force gauge and two vent grooves to release the trapped gas during vacuum.
6) The **EP60 plates** are two stainless steel pieces designed to attach the aluminum structure to the guiding linear unit EP 60.
7) The **Frame Plate** is a stainless steel piece designed to attach the aluminum structure to the bottom flange.
8) The **Mounting Axe** is an aluminum cylinder with a head on one side. The mounting pieces are only used to position the pulling rods inside the vacuum cell while assembling the structure or placing a sample to test. The mounting axe focuses the position of the mounting mandrel through the mounting flange. They are not used during the thermo-mechanical test.
9) The **Mounting Flange** is a Hositrad ISO-K 100 Blank Flange with a hole in the middle for the mounting axe.
10) The **Mounting Mandrel** is an aluminum piece used to calibrate the position of the up and bottom pulling rods.
11) The **Bottom Piezo Attach** is a stainless steel piece which is set to the bottom end of the piezoelectric actuator. It fixes this one to the frame through the piezo plate.

12) The **Top Piezo Attach** is a stainless steel piece which is set to the top end of the piezoelectric actuator. It fixes this one to the bottom stub, which is fixed to the bottom pulling rod.
13) The **Bottom Pulling Rod** is a stainless steel piece which is fixed to the bottom stub and the bottom sample holder.
14) The **Top Pulling Rod** is a stainless steel piece which is fixed to the force gauge and the top sample holder.
15) The **Sample Holders** are two stainless steel pieces that hold the sample.
16) The **In Spring Rods** are three pieces that hold the inner washer to guide the bottom pulling rod and hold it when no tension is applied.
17) The **Out Spring Rods** are three pieces that hold the outer washer to guide the bottom piezo attach and hold it when no tension is applied.
18) The **In Spring Washer** is a stainless steel piece that rests over three springs guided throw the spring rods and holds the bottom pulling rod.
19) The **Out Spring Washer** rests over three springs guided throw the spring rods and holds the bottom piezo attach.
20) And 21) **Supports** hold the infrared radiators inside the vacuum cell.
22) The **Piezo Jumpers** are two pieces that hold the piezoelectric actuator to both the bottom and top piezo attach.
23) The **Piezo Plate** fixes the guiding linear unit EP 60 to the tensile structure.

3.3 Vacuum structural components

Here are included all vacuum structural components. The modified components are included in the previous chapter and can also be found in the ANNEX B.

Elements 100LF	Qty.
ISO-K 6-way cross	1
ISO-K weld flange	1
ISO-K blank flange	4
ISO-K 100 to 40 adaptor	2
ISO-K viewport zerolength glass	1
ISO-K centering ring	6

Elements 40KF	Qty.
NW40KF clamping collar	3
NW40KF 20 pins connector	1
KF centering ring NW40KF	4
KF Reducer tee 40-16	1
NW40KF block valve	1

Elements 25KF	Qty.
NW25KF clamping collar	1
KF face clamp NW25 KF	2
W25KF blank stub stainless steel	3
KF centering ring NW25KF	4

Elements 16KF	Qty.
NW16KF 3 thermocouple feedthrough	1
KF centering ring NW16KF	2

Elements 63-100	Qty.
ISO-K single wall clamp stainless steel	10
ISO-K double claw clamp stainless	6
ISO-K double claw clamp aluminum	34

Table 3.2: Vacuum components from different flange sizes.

3.4 Structure set up

The frame set up instructions finish with the frame plate and EP 60 unit installed although there is no explanation in that particular chapter. So the first step in this set up is fixing both plates to the aluminum structure.

The frame plate is attached with 28 screws to the central part of the structure.

The EP60 plates are attached to the central reinforcement with 9 M6 screws each one of them. Afterwards, the EP60 linear unit must be fixed to these plates with the screws supplied together with the unit.

Further instructions assume the vacuum components have been properly cleaned and the operator is taking the required measures to avoid depositing dirt and grease on the pieces.

The top stub and the force gauge through the top flange are hence to be fixed. The load cell (or force gauge) is symmetrical so there is no specific orientation for it. The exact distance that should be left between the nut and the end of each of the screws in the load is 8.6mm. From a practical point of view, no distance can be so precisely fixed with such a nut, so a distance between 8.6 and 9mm is enough.

- When screwing the top stub to the load cell block the nut with a wrench.

Leaving the same distance between the bottom nut and the end of the screw, attach the top pulling rod to the gauge, taking care again of not moving the nut while doing this.

Three key requirements have to be taken into consideration for the previous step:

- The load cell wired has to be finally oriented in the radial direction to the center of the flange.
- The top pulling rod groove has to be finally oriented perpendicular to this direction.
- The vertical extension of the whole set of pieces has to be appropriate for the mounting mandrel to fit.

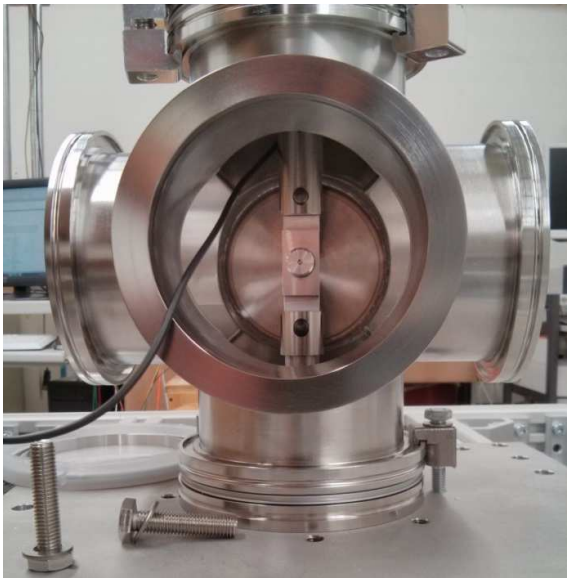

Figure 3.6: Mounting mandrel attached inside the 6-Way-Cross.

Only after these are checked should the clamps be placed to tight the stub against the flange.

Once this top assembly is done, the bottom flange has to be fixed to the bellow using clamping pieces and the four screw holes made to this end. Afterwards, the bottom stub must be fixed to the bellow using a clamping collar.

The bottom flange must be then placed on the frame plate. Then the inner spring rods, with the inner washer and the bottom pulling rod can be set in position. Pushing the bottom stub gently with one hand can one then screw the bottom pulling rod into the stub.

- As in the top pulling rod, orient the groove in the same direction.

The linear unit EP60 should be then attached to the piezo plate. Following, the outer spring rods, with the springs, the washer and the bottom piezo attach must be fixed, analogous to the inner spring-rods-washer operation. After the top piezo attach is screwed to the bottom stub, fix the piezoelectric actuator to the assembly using the piezo jumpers and adjusting the position of the linear unit.

As can be seen in Figure 3.6 adjust the position of the whole bottom assembly with the EP60 so that the mounting mandrel can be properly fixed to the bottom pulling rod.

4 Electric systems

The electric systems are all the components of the machine which are not structural or from the tensile structure. They are responsible for the tensile force, the vacuum and temperature conditions and the data acquisition. Most of these systems require one or more components inside or in contact with the vacuum cell.

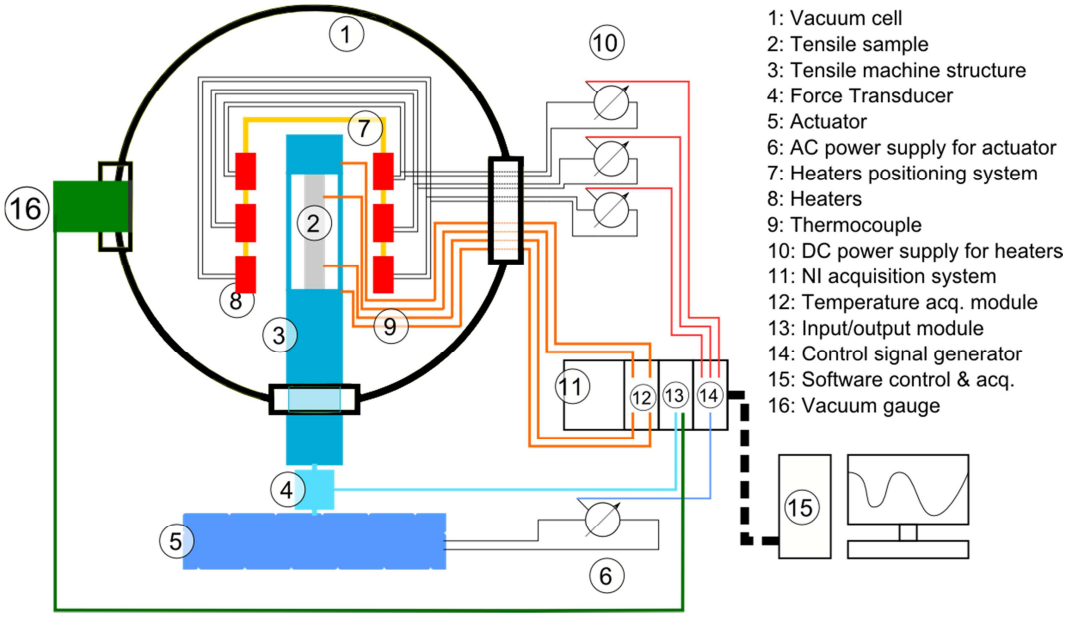

Figure 4.1: Scheme of the electric system.

It gives an idea of the basic elements that compound the systems of the machine. The whole electric scheme is represented in ANNEX C.

The power supplies for the radiators are actually installed in an electric box together with the power supply for the vacuum gauge. This electric box is represented in Figure 4.8 and can be seen in Figure 4.7.

4.1 Force system

It is composed mainly by a force actuator and a force sensor. As the rest of electronics systems, it is controlled via computer LabView interface through the National Instruments equipment. The structural elements of the force system have previously been described.

4.1.1 Piezoelectric actuator APA 1000L

The actuator APA 1000L is formed by several ceramic low-voltage actuators, MLA or Multi-Layer Actuators. Amplification of force takes place thanks to an elliptical shell which magnifies force in the small axis from the deformation applied to the longer axis. The shell also protects the APA 1000L from mechanical stress.

The actuator receives input power from the CA-45 compact standalone amplifier, which is in turn controlled by the NI-DAQ.

The force will be monitored by the force transducer inside the actuator as well as an independent load cell: the U9B force transducer.

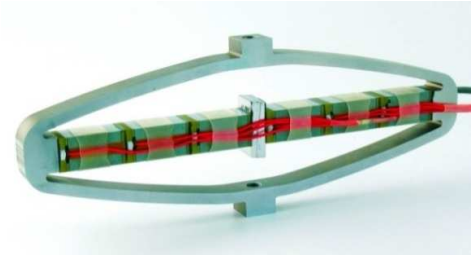

Figure 4.2: Piezo electric actuator 3D model.

4.1.2 CA 45 Compact standalone amplifier

The CA45 is a bipolar (-20 / +150 V) low cost and low noise compact single channel linear amplifier for driving low voltage piezoelectric actuators. It is a standalone one channel amplifier encased in a RK12 small rack, and can be equipped with feedback sensors in order to provide a closed loop control.

Thereupon there will be no closed loop force control system programed in the LabView software, as the CA-45 includes itself a built-in control system.

4.1.3 U9B Load cell

The U9B force transducer permits measuring static and dynamic lineal strain with virtually no displacement. The stress applied to the transducer is transmitted to the piezoresistor inside it. This resistance can be measured through a Wheatstone bridge, powered at 10V from the outside.

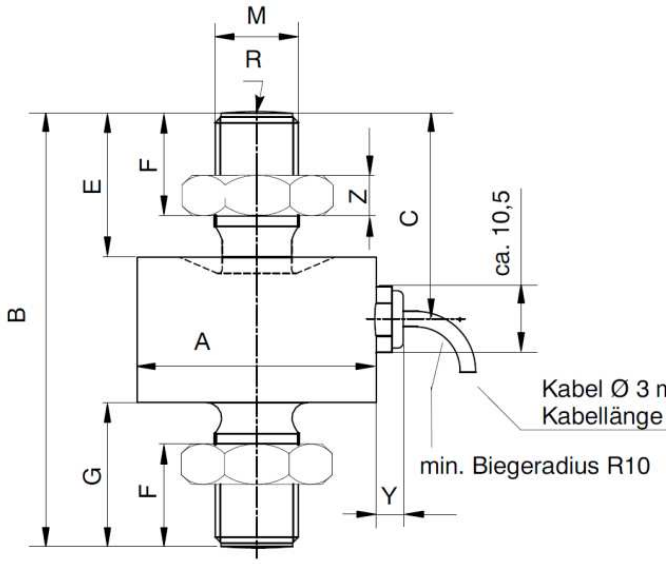

Figure 4.3: Load cell.

Dimension	Value
A	26
B	60
C	28.5
E	21
F	16
G	21
M	M10
R	40
Y	Ca 5.5
Z	**5**

Table 4.1: Load cell dimensions.

4.2 Heating system

The need to heat up to moderately high temperatures at vacuum justifies the choice of infrared radiators as heating source. This demanding design condition turns the heating in the most complex system of the machine.

- Six infrared radiators are used for heating the sample inside while testing.
- Vacuum wire
- A special 6 pin thermocouple K adapter is used to penetrate the thermocouples inside the vacuum cell.
- 12 out of 20 pins of a wire adapter are used to penetrate the power inputs of the radiators inside
- Three out of four power supplies in the electric box supply the thermocouples. Each one supplies two infrared radiators.

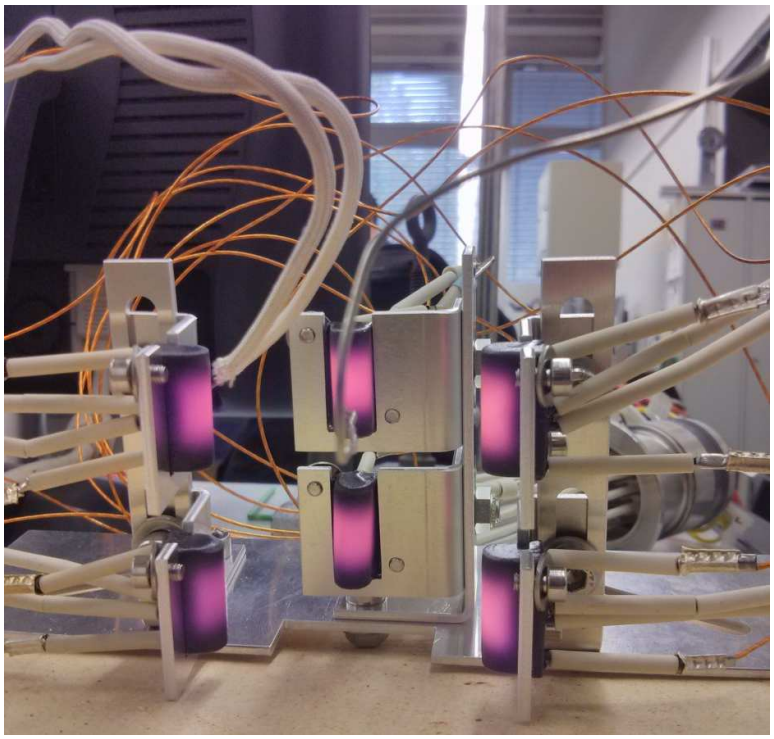

Figure 4.4: Infrared radiators assembled.

4.2.1 Infrared radiators

Six infrared radiators are used for heating the sample inside the vacuum cell while testing. Each couple of radiators is powered by a power supply. Each one of the radiators is protected by a 5A rewire able fuse.

Figure 4.5: Infrared radiator with in-built k type thermocouple.

Figure 4.5**Error! Reference source not found.** shows one of the infrared radiators being tested. The centre pins correspond to an internal thermocouple and the external pins correspond to the power input. The picture was taken from the first time in which the temperature control system was tested. The temperature measured from the thermocouple indicates that the radiators are able to reach temperatures higher than 800°C with atmospheric conditions. This temperature was achieved applying full 55W to the radiator, which is the max working power in agreement to the datasheet.

When the tests in vacuum began, it will be necessary to monitor the temperature of at least one radiator to be sure it remains under acceptable limits (900°C). Due to the absence of convection convection it is expected to reach much higher temperatures with the same power input.

4.2.2 SITOP flexi Power supply

Each power supply Siemens SITOP Flexi can feed two of the radiators. Three power supplies are needed to give power to the six infrared radiators. The maximum intensity and the voltage are controlled by two different terminals which are connected to the NI-DAQ.

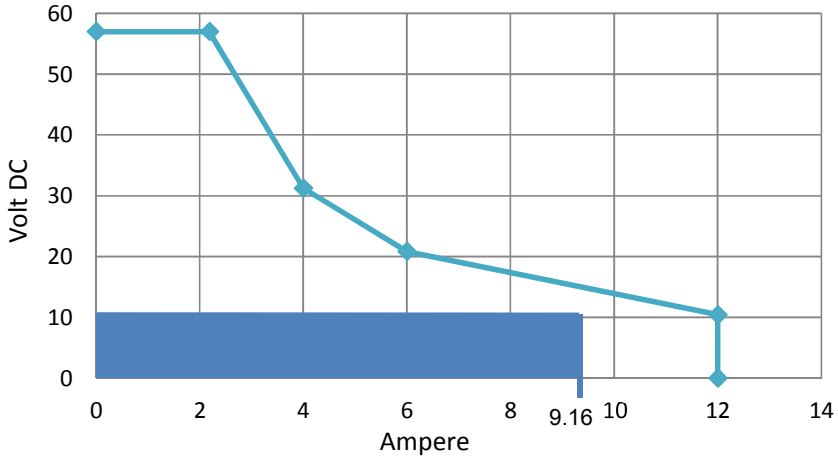

Figure 4.6: Power curve of the SITOP flexi. The dark blue area corresponds to the possible range of values for the voltage and current.

The maximum power deliverable by a SITOP Power Flexi is set at 120 W. However, as shown in Figure 4.6, the maximum power spot is set at 11V and 9.16A; this means 11V and 4.58A at the radiator's terminals. This configuration is appropriate to leave some margin to the maximum power using 5A fuse.

The SITOP allows controlling voltage but not intensity. Current can only be limited to a certain maximum value; the real value would be determined by the load and the voltage.

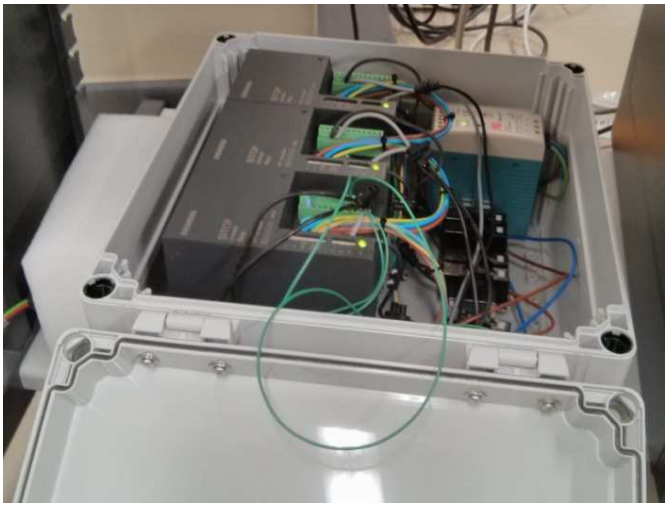

Figure 4.7: Electric box including three SITOP and one RS 428-477 power supplies.

The full electric scheme can be seen in the ANNEX C. The 5A rewire able fuses are installed also inside of the electric box. The green wires send the analog signal from the National Instruments equipment to the power supplies. All of them are wired to the same signal so the power of the radiators cannot be established separately.

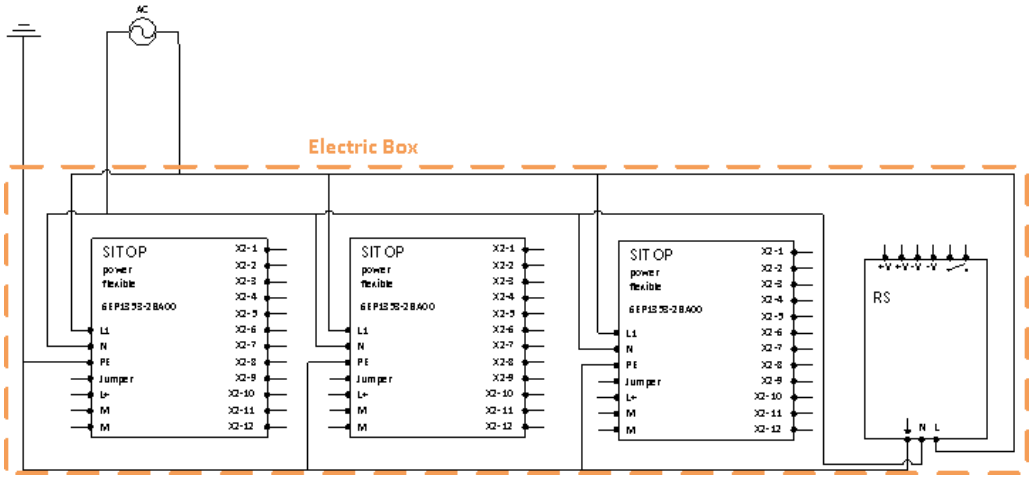

Figure 4.8: Scheme of the electric box.

4.3 Vacuum system

The vacuum system is needed to provide a chemically inert atmosphere during the test. Usually there are two ways of providing this, with vacuum or with a noble gas atmosphere. In this case, vacuum is just right for the test, as the pressure during the test is not a conditioning.

The elements that compose the vacuum system are a vacuum pump, a vacuum gauge, the vacuum pipes and the vacuum cell.

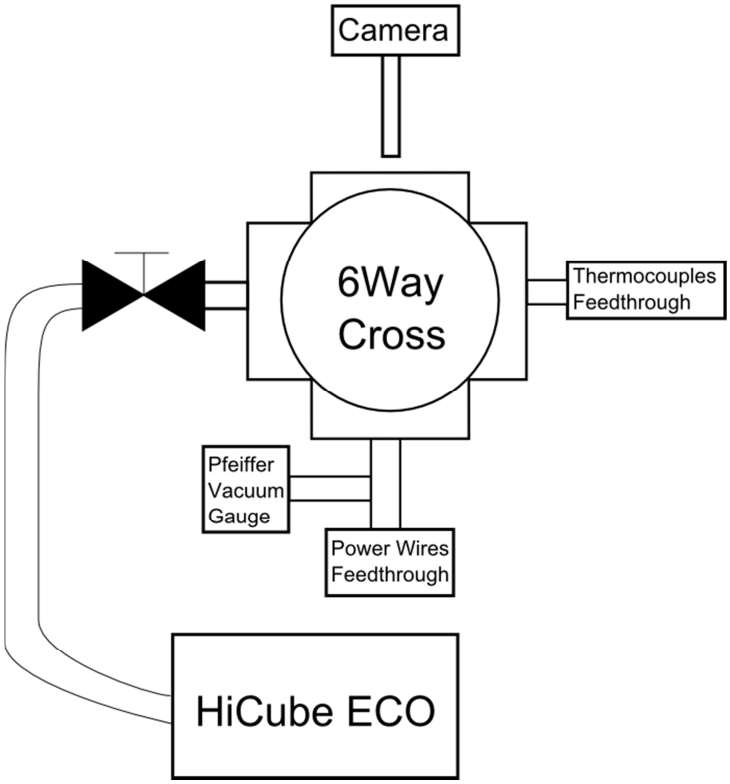

Figure 4.9: Vacuum system scheme.

Figure 4.9 shows a schematic top view of the vacuum cell main parts seen from the top. The front flange is reserved as windows for the camera. Another side is occupied by the connection with the vacuum pump through a vacuum hose. This connection is separated by a valve that can isolate the pump from the vacuum cell. The vacuum gauge as well as all the wires and thermocouples go through the back flange of the vacuum cell. The last flange has no connections, it is used to install and move all the components inside the machine.

4.3.1 HiCube 80 ECO ISO-K

The pumping station HiCube ECO is a series set-up of two different pumps. Typical vacuum installations have at least a low and a high vacuum pump which operate in series. In this case both are configured as a single machine that can pump from atmospheric pressure to 10^{-7}mbar. The MVP 015 is a diaphragm pump that creates the adequate pressure for the turbo pump to work. It can reach pressures under 0.5mbar.

The HiPace80 is a turbo pump which profits from the vacuum created by the MVP 15 to reach pressures under 10^{-7}mbar. It needs as much as 22mbar in the exhaust operating with air or N_2. The whole system is controlled through a digital interface called DCU.

In *Figure 4.10* both the turbo pump (metallic, on top of the structure) and the diaphragm pump (red, inside the frame), can be distinguished. Pfeiffer guarantees pressure levels under 10^{-7}mbar. Tests in the laboratory after 48 hours of operation have achieved up to $9.6x10^{-8}$ mbar.

4.3.2 Pfeiffer compact full range PKR 251

The Pfeiffer Compact FullRange, as seen in

Figure 4.11, is a vacuum gauge compound by two different measurement technologies, depending on the pressure range. As it happens with the HiCube 80 ECO both technologies are combined in such a way that for the user, they behave as one single measurement system.

Figure 4.10: HiCube ECO Turbo pump.

Figure 4.11: PKR 251 Vacuum gauge.

The pirani-gauge works alone in the range between 1000mbar and 10^{-2}mbar, and together with the cold cathode gauge. The working principle is based on a heated metallic wire suspended in vacuum. The heat power lost to the atmosphere is related with the density of the gas inside i.e. vacuum.

The cold cathode gauge works discharging electron currents with such a high voltage (around 2kV) so that it can continue at very low pressures. This is attained by the use of a magnetic field to make the paths of the electrons so long that their collision probability with gas molecules is sufficiently large to maintain the discharge on the formation of the required number of charge carriers.

4.3.3 RS 428-477 Power supply

The RS 428-477 feeds the PKR 251 with a DC voltage of 24V.

Figure 4.12: Power supply RS 428-477.

4.4 Control system

The control system is in charge of controlling the heating system, the force system, and registering the data from the vacuum system. There is no control loop here for the vacuum, the pump is set on analogically and the gauge sends the pressure info to the computer.

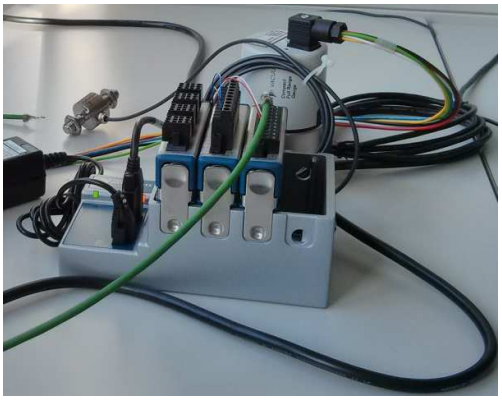

Figure 4.13: National Instruments cDAQ-9174 USB chassis.

The National Instruments cDAQ-9174, as can be seen in Figure 4.13 is a chassis connected to a computer via USB that includes four slots for different Data- Acquisition cards.

Figure 4.14: NI-9219 module.

Figure 4.15: NI-9263 module.

Figure 4.16: NI-9211 module.

- The NI-9219 is a multipurpose testing module designed to register information as well as output voltage excitation levels of 2.5V. This card is connected to the output of the vacuum gauge and one of the thermocouples.
- The NI-9263 is a 4-channel analog output module. Works on the ±10V range and is responsible for the input signal of the infrared radiator's power supply, the input signal of the piezoelectric actuator and the excitation signal of the force transducer.

- The NI-9211 is a thermocouple input module able to read 4 voltage differences simultaneously. Three thermocouples connect the NI-9211 to the sample and the fourth slot is reserved for the force sensor output signal. The reason to use the last slot for the force transducer is the higher resolution compared to the NI-9219. This cad is equipped with a thermistance to measure the temperature at the cold junction.

Figure 4.17 shows how the information moves through the machine. The 6 way cross and the vacuum components are seen from a top view.

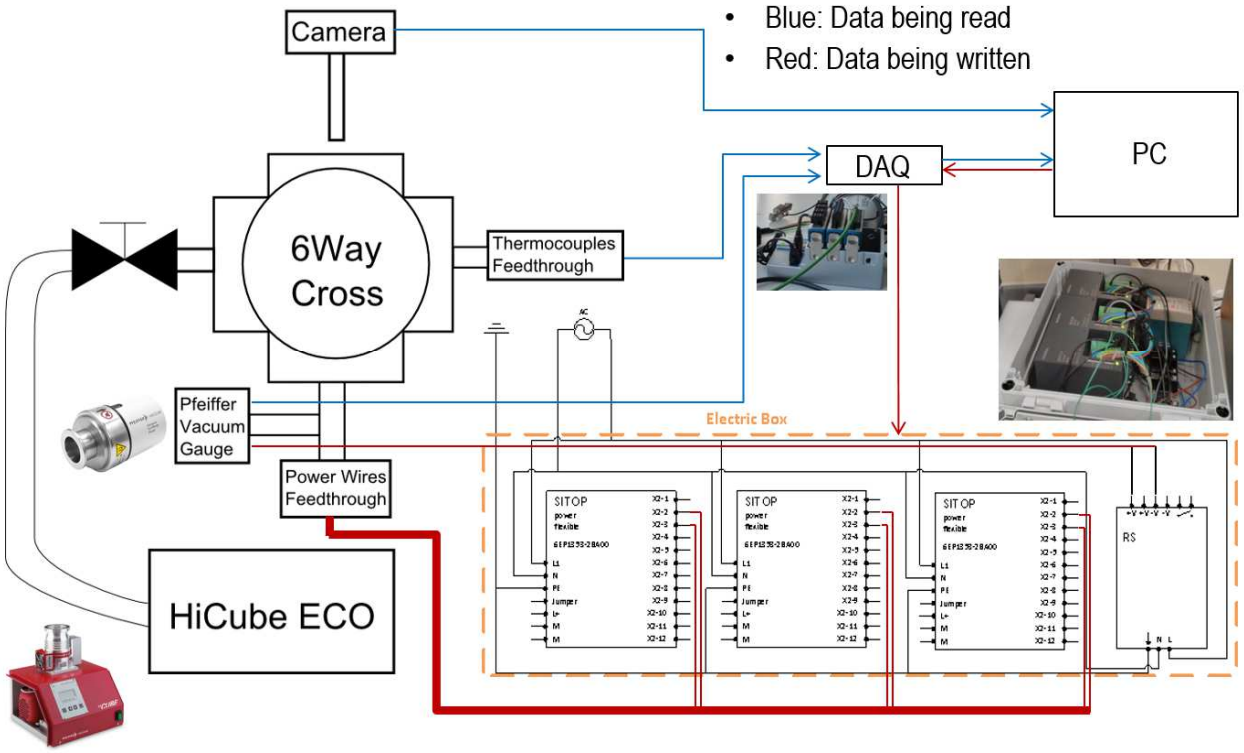

Figure 4.17: Data flow scheme of the machine.

4.5 Optical system

The optical equipment is composed by a camera and a telecentric lens. The Acquisition of the images is made via USB 3.0 in the same computer that controls the rest of systems. The software used for this purpose is distributed by BASLER to be used specifically with BASLER digital cameras.

Figure 4.18: BASLER acA2500 um.

Figure 4.19: Edmund Optics 63743.

4.5.1 BASLER acA2500 um Camera

Thanks to the USB 3.0, the acA2500 um provides fast image acquisition and power supply with a single cable.

Resolution	2592 x 1944
Sensor	CMOS
Pixel Size (µm)	2.2 x 2.2
Frame rate (fps)	14 fps

Table 4.2: Characteristics of the camera

4.5.2 Edmund Optics 63743

It is a telecentric lens with 6.0x main magnification and focal ratio 35.0. A telecentric lens is necessary as the objects do not change their size with distance as seen in Figure 4.20.

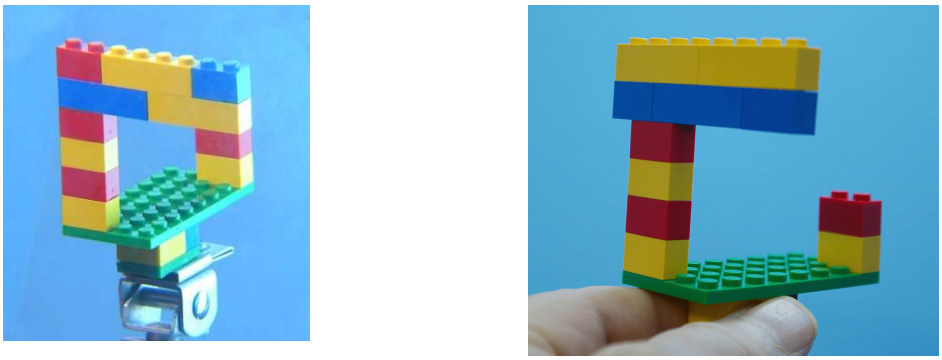

Figure 4.20: Optical effect created by the use of a telecentric lens.

5 Software

5.1 LabView

The National Instruments LabView Suite 2013 is a graphic programming interface which can be easily programmed to simulate, read and control all kind of laboratory hardware, by creating virtual instruments. The tasks for this project are:

- Control of the heating system with a PID controller
- Control of the force system
- Aquire the temperature, force, pressure and time
- Give on-time overview of the performance

A vi is the type of file for programs made with LabView. The LabView project which includes all the Vis is TensileTestingControl.lvproj. Inside, the now on called “program” is the MainControl.vi.

5.1.1 Graphical Interface

The graphical interface of the program is clear and intuitive. The main part of the window is divided in three tabs: temperature, force and pressure.

The rest of it is reserved for the common elements of the three of them. Once the operation with the machine starts, further elements can be added to this section. By now only a Stop button and an Execution Time indicator can be found here.

This execution time shows the time between the current execution of the algorithm and the previous one. In normal operation this time should be 511ms.

The stop button is recommended to be used instead of the LabView stop button. The physical channels are cleaned this way.

In the temperature control tab, there is a large graphic chart showing the evolution of temperature as measured by the thermocouples. The information shown can be selected in this case.

The “Temperature Set” and “Temperature Rate” control variables are self-explanatory. Once

introduced the data, the program creates a slope with the required speed and set point.

- There is a remark regarding the OK button. It has to be pressed twice every time in order to start the execution of the task.

In the force control tab the configuration is pretty similar as in the temperature tab, although no controller is programmed in this section for the temperature. This was already exposed in the force system explanation.

The pressure tab has only a single graphic chart with the evolution of pressure through time.

- It is recommended to "clear chart" in the pressure tab to rescale the graphic every so in a while.

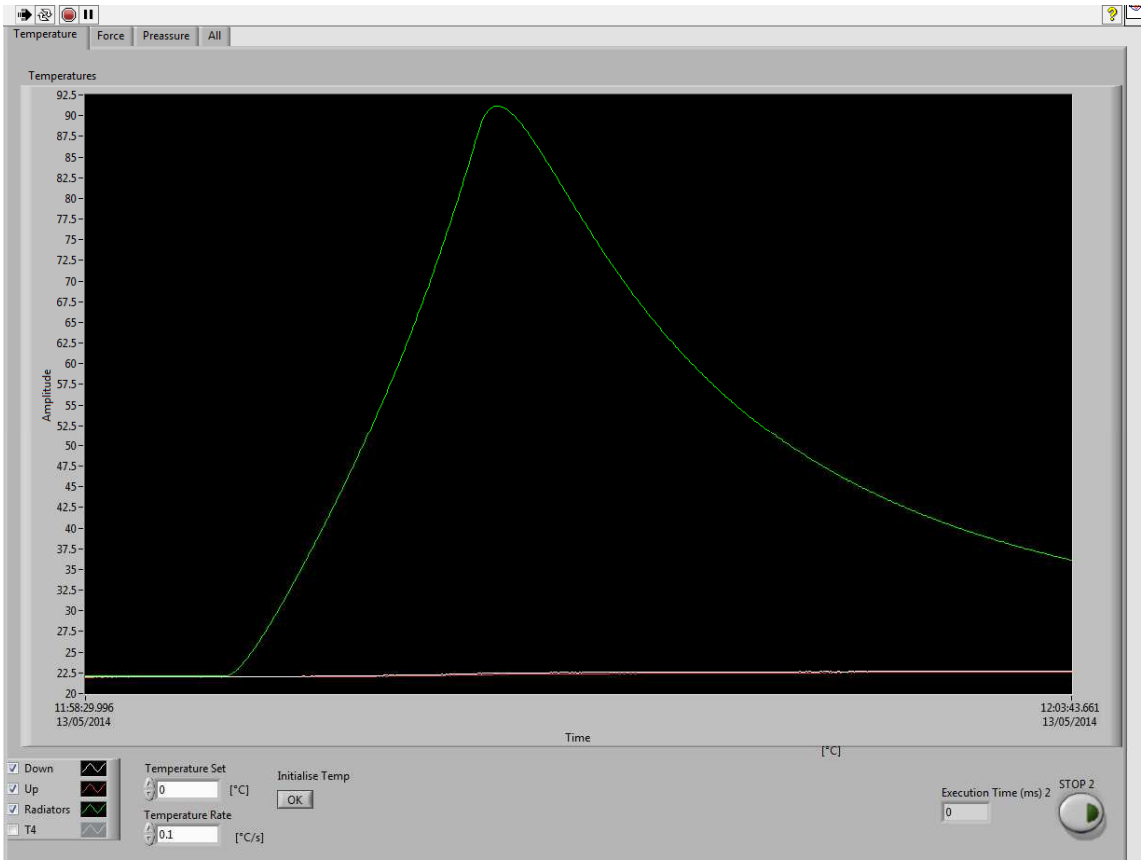

Figure 5.1: Graphical interface of the temperature tab while testing the radiators and thermocouples.

5.1.2 Block Diagram

The MainControl.vi is divided in three while loops:

- Data Acquisition or DAQ loop
- Temperature control loop
- Force control loop

This division could possibly not look like intuitive in a program which is made to be easy to use and understand. A first version of the same program was made building small programs with pressure, temperature, force and data divisions. However it is not practical for several reasons.

The first reason is the use of the DAQ assistants. They simplify greatly the task of taking and sending data to the hardware, but they are slower than a manual physical channel configuration. The initial idea of the NI-cDAQ chassis was more compatible with an easy understanding of the program, because each module was focused in one system. The thermocouple module tested temperature, the multi-purpose module tested and excited the force system and the vacuum gauge, and the output module gave power to the thermocouples. After first experiences, the configuration suffered several changes.

The multi-purpose module, even with the highest excitation (10V), does not have enough reading resolution to read the force gauge tension output, whereas the thermocouple module does. Therefore at least one thermocouple slot had to be reserved for the force gauge, which means this module is not temperature-system exclusive anymore.

Mixing systems in the different hardware modules is problematic, because the DAQ assistant does not permit reading information from the same module while other DAQ assistant is reading. So the structure of the program has to be centered on the input/output information system rather than in a system-divided way.

5.1.2.1 Main structure

The program initial processes set up the configuration for the file where the data will be written during operation. Once you turn on the program, it asks you if you want to create a new log file or overwrite one already existing. The WriteFirstLine.vi writes the first line of the data to identify the information in each column. Also writes the name of the user for this session, which is asked after the log file is selected/created.

Once this is initialized, the program will write the data every loop. This approach does not offer the fastest performance, but allows recovering the data from the test in case of unexpected power shutdown.

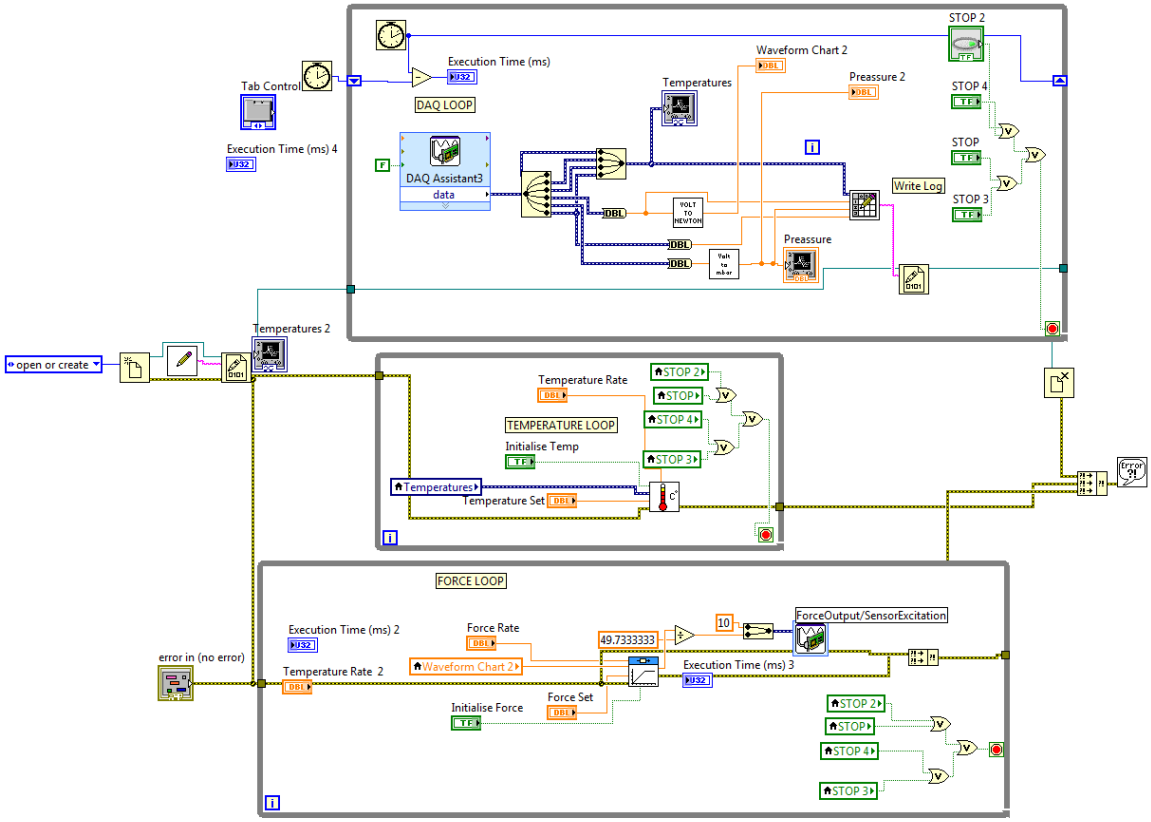

Figure 5.2: Block diagram of the main body of the program.

5.1.2.2 DAQ loop

All the information from the hardware is read in this loop. Pressure and the force are then converted to mbar and newton afterwards, and send together with the temperature data to the graphic charts. The graphic chart of the temperature is at the same time a local variable which is sent to the temperature control loop. The temperature is sent to the WriteLine.vi in the form of a merged signal, which is separated again inside the VI and transformed to string type. The force and pressure data are introduced in the WriteLine.vi too, later transformed to string type and all concatenated together to form a single string which is written in the log file. In this loop there is also the execution time "device". It subtracts the clock time of the previous iteration with the clock time of the current iteration.

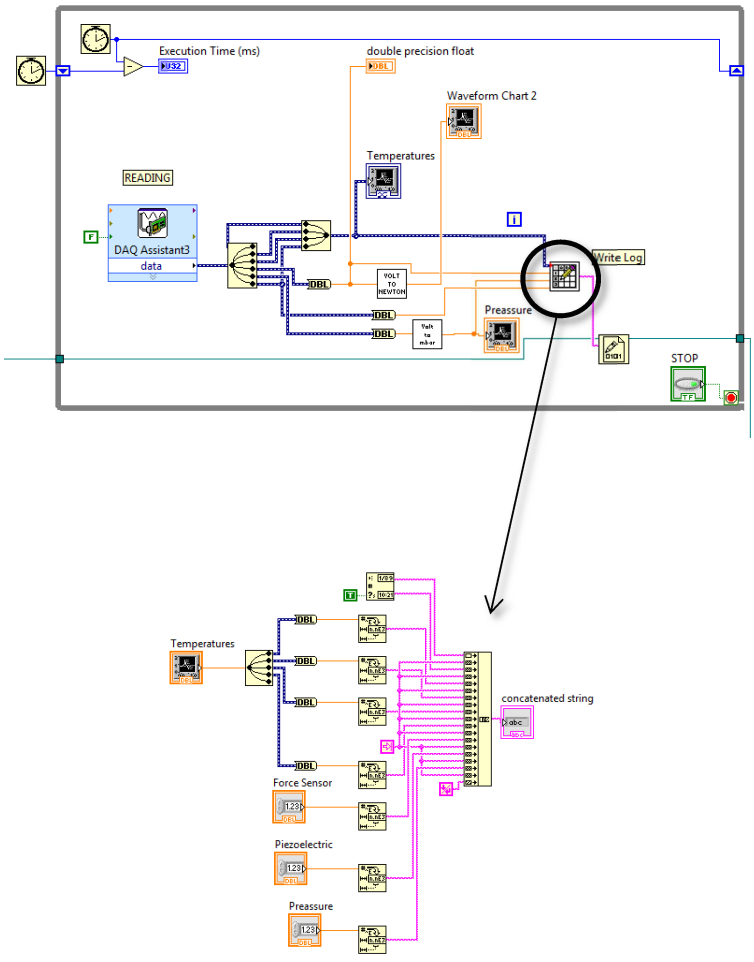

Figure 5.3: DAQ loop and magnification of the WriteLine.vi.

5.1.2.3 Temperature control loop

This loop is used to control the temperature through a PID in the TemperatureControl.vi. The loop receives the set and the rate of temperature from the interface and the current temperature from the local variable.

The TemperatureControl.vi creates a slope through the setpointramp.vi using the variables “temperature set”, “ramp rate” and the current temperature. The ramp output is sent to the set point of the simplePID.vi, together with the current temperature as process variable. The values of the Kp, Kd and Ki values have been set empiricallz. The lower limit is set to 0 and the upper limit is set to 1.1538 volt, which is equivalent to 11 volts in the power supplies output. Finally the output of the simplePID.vi is sent to the output DAQ assistant who sends the voltage signal to the SITOP power supplies.

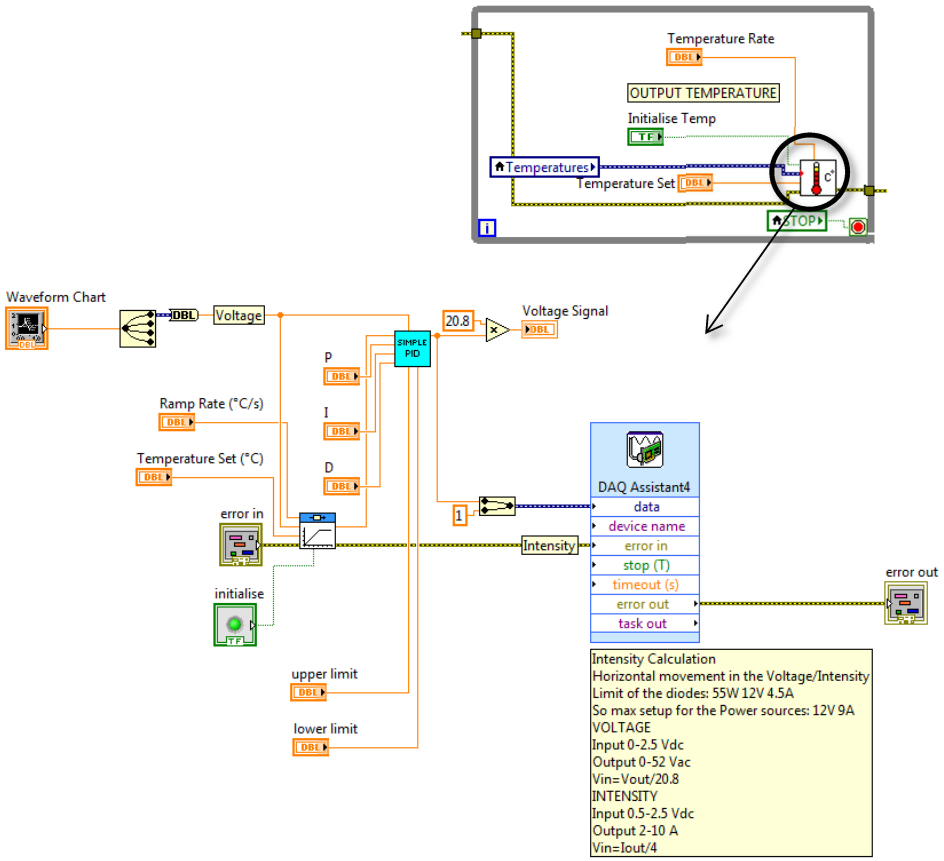

Figure 5.4: Temperature control loop and detail of the PID controller.

5.1.2.4 *Force control loop*

The force control system uses an open loop control. The signal is created by another setpointramp.vi using the desired change rate and the set point. As usual, the output of the slope is sent to the DAQ assistant who in-turns sends the signal to the power controller. Merged with the signal before the DAQ assistant, a signal of 10V is required as excitement for the force gauge to work.

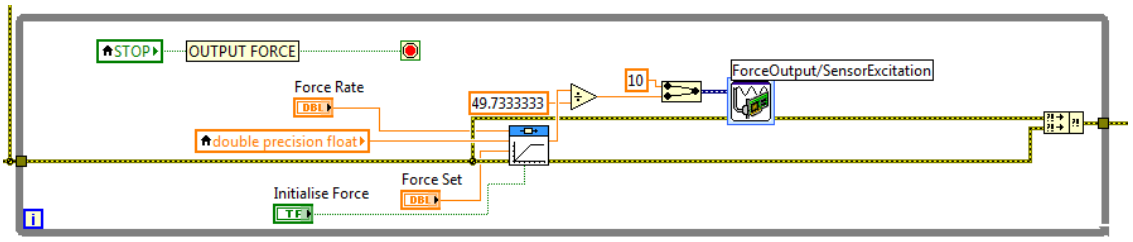

Figure 5.5: Force control loop.

5.2 Digital Image Correlation

The Digital Image Correlation system estimates the deformation on the surface of the sample by finding the displacement field between too pictures. The pictures are taken by the camera through a glass in the side of the vacuum cell and sends them to the computer. The vacuum cell had been previously modified to shorten the distance from the sample to the camera.

"Improved Digital Image Correlation" is the Matlab Code used during the experiments. This code has been programmed by Elizabeth Jones, from the University of Illinois at Urbana-Champaign[7].

5.2.1 Interface

There are four main GUIs inside this code. Each of them is accessed by typing the name in the command bar and should be called only after the previous GUIs have been succesfully used. All the images prepared to be correlated must be placed in the same folder as the program before starting the correlation.

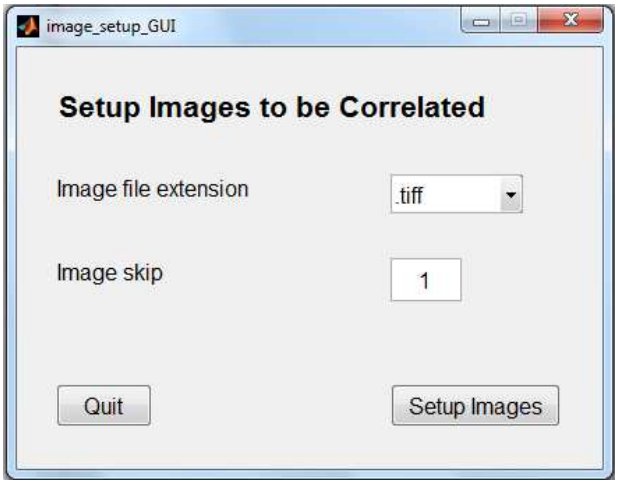

Figure 5.6: image_setup_GUI prepares the images for correlation. Skip number can be changed to reduce the number of images to correlate.

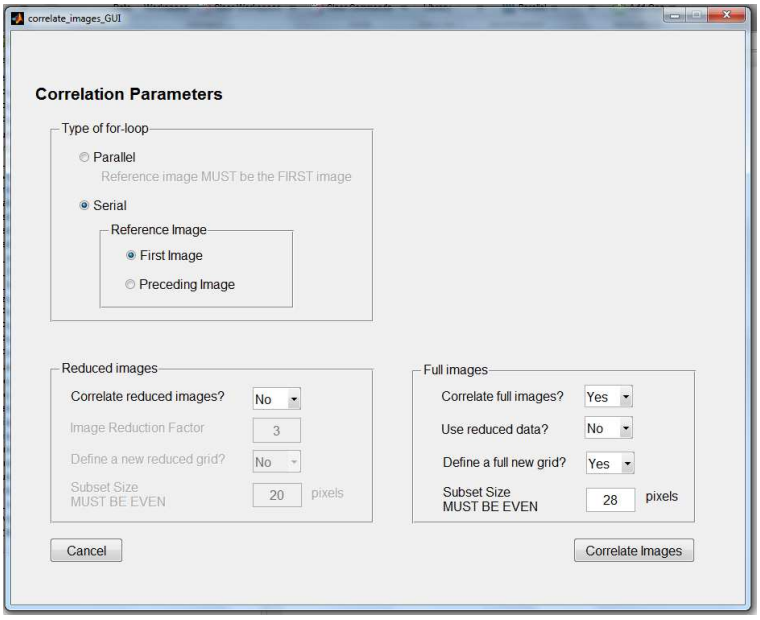

Figure 5.7: correlate_images_GUI performs the image correlation and calculates the displacements.

Using the parallel implementation of for-loop can save time in case of having a multi-core CPU in the computer, and having the *Parallel Computing Toolbox* for Matlab. The reference image gives the choice to correlate always the pictures with the previous one or with the original one.

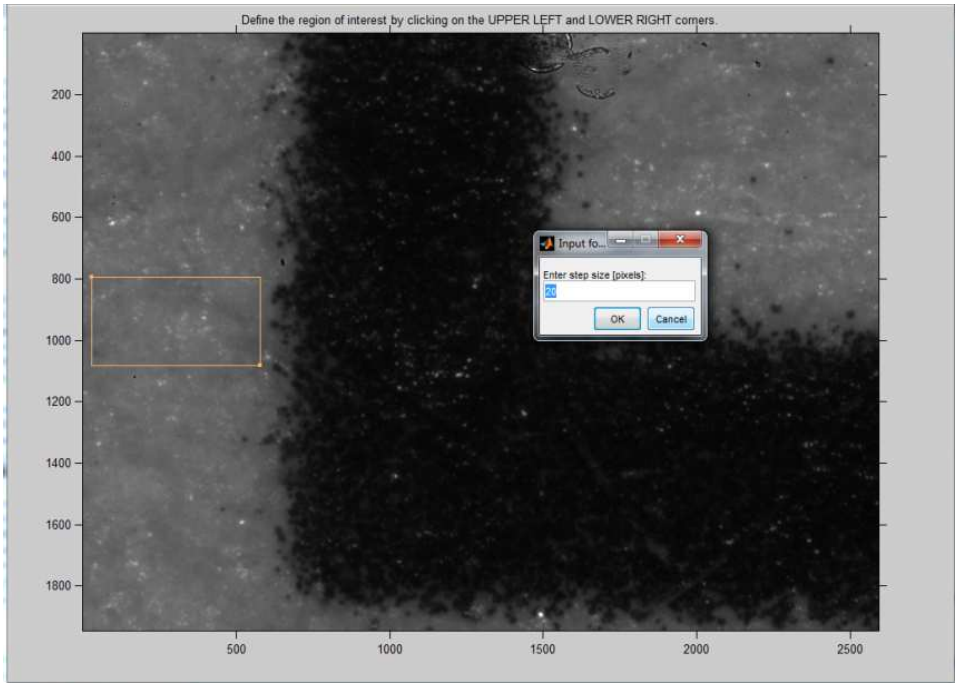

Figure 5.8: Area selection for correlation and step size between elements.

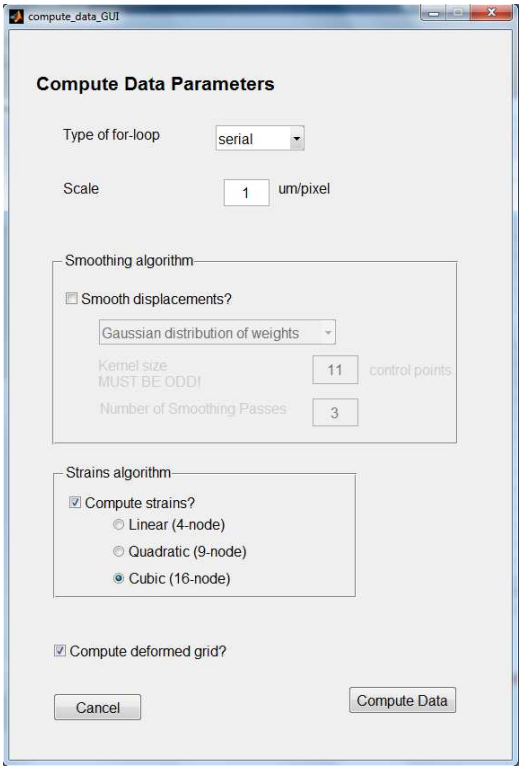

Figure 5.9: compute_data_GUI: Smooths and interpolates displacements, calculates strains using finite element shape functions.

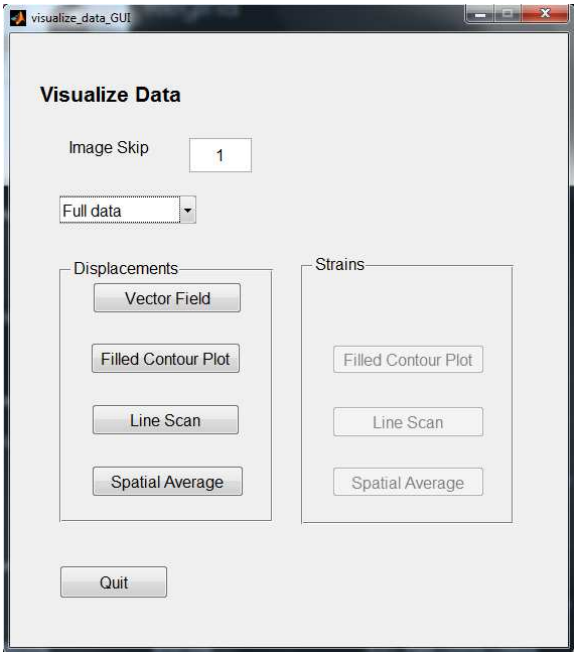

Figure 5.10: Creates different types of graphics to visualize the data. It permits showing it as a vector field (displacements only), a filled contour plot, a line scan, or a spatial average.

6 Qualification

Before further experiments are performed, limitations on the optical capabilities of the prototype have to be taken into consideration. This is referred not only to the camera and image acquisition system but also the error which is expected from the DIC software.

6.1 Optical system characterization

The optical equipment is characterised by the angular resolution, which sets the minimum angle between objects the optical system can successfully distinguish. The Rayleigh's criterion sets the size of the minimum resolvable object for an optical system due to light diffraction and depending on the wavelength of the same and the diameter of the lens.

Objects separated the Rayleigh criterion or further can be distinguished from each other.

$$\theta = 1.220 * \frac{\lambda}{D} = 1.220 * \frac{700 * 10^{-6}}{\frac{65}{35}} = \\ = \mathbf{4.5984 * 10^{-6}}\ rad$$

- λ is the wavelength of light.
- D is the effective diameter of the lens and is equal to the ratio of focal length to f-number.

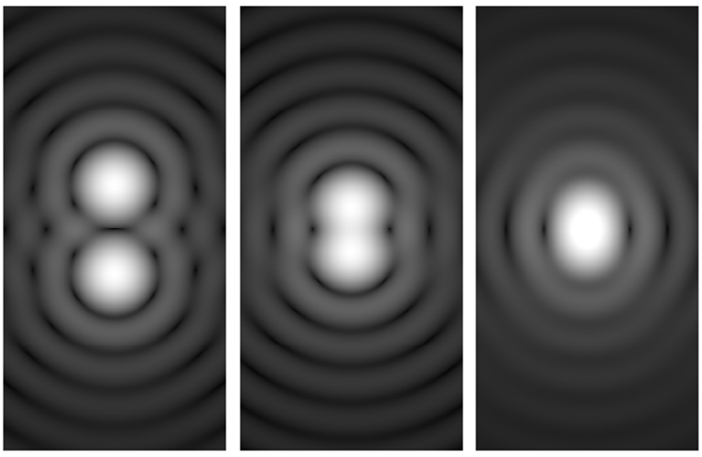

Figure 6.1: Example of the Rayleigh's criterion. The distance between the two objects is equal to the Rayleigh's criterion in the middle picture.

6.2 Spatial resolution

Testing the real performance of our camera-lens system is a necessary procedure to know its degree of reliability. To that end, a printed sheet of paper is used as a sample and it is optimally focused and illuminated, as shown in Figure 5.12.

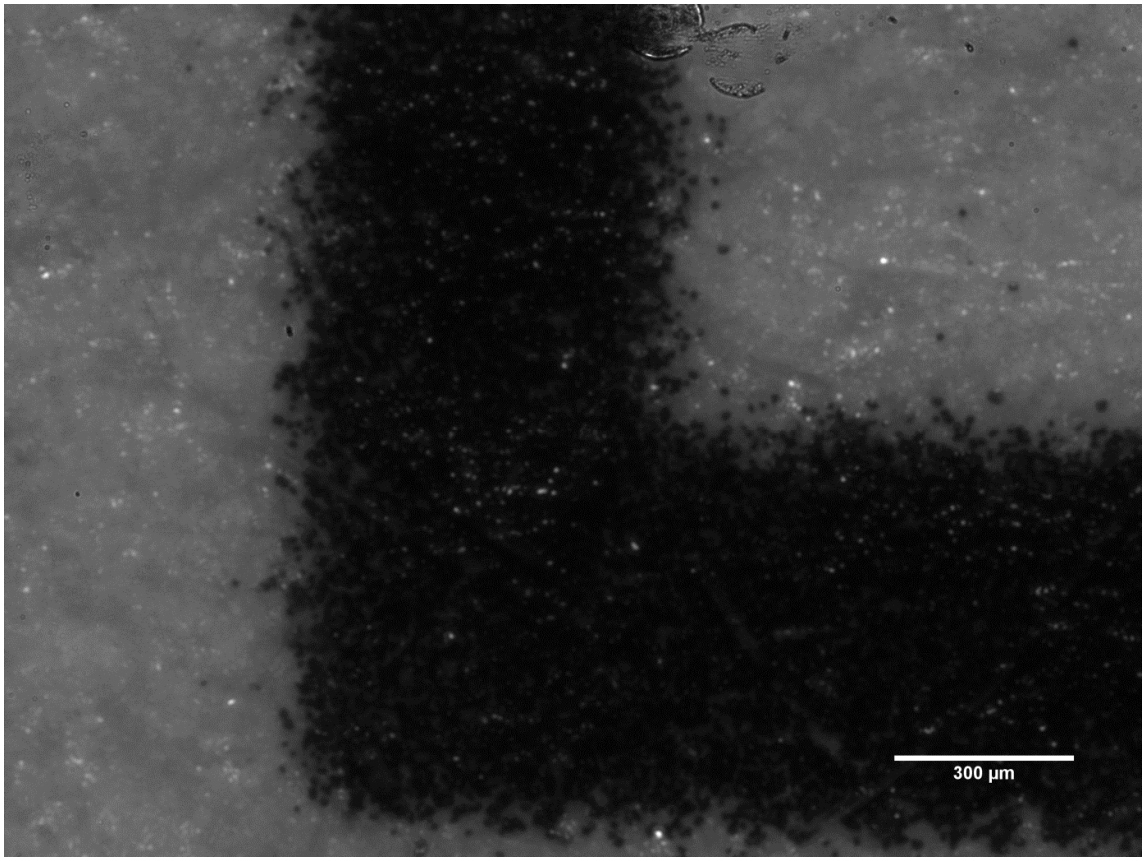

Figure 6.2: Picture of a printed text used as a target for optical and digital calibration.

Afterwards, the picture taken is analysed with ImageJ to determine the resolution. The gray level variation is evaluated along a line located such that it crosses an interface between a dark object and the light grey background. This measurement gives an idea of the amount of pixels it takes to identify two different objects with the optical system. The line used for the analysis can be seen in Figure 6.13. The transition appears in Figure 6.14 with an approximate value of 15 pixels. The conclusions following are the empirical estimated minimum resolvable object for this optical system.

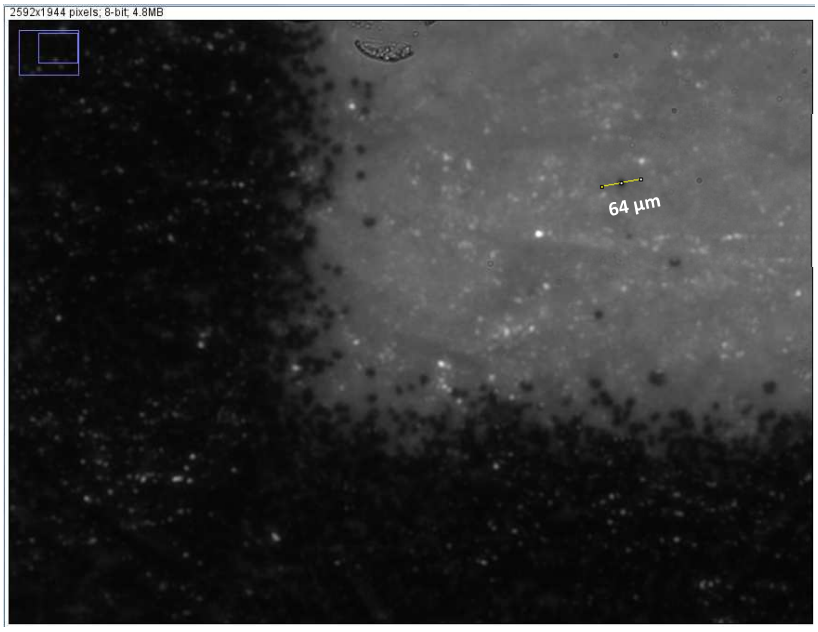

Figure 6.3: Magnification of our target. The yellow line shows the spot used to test the resolution.

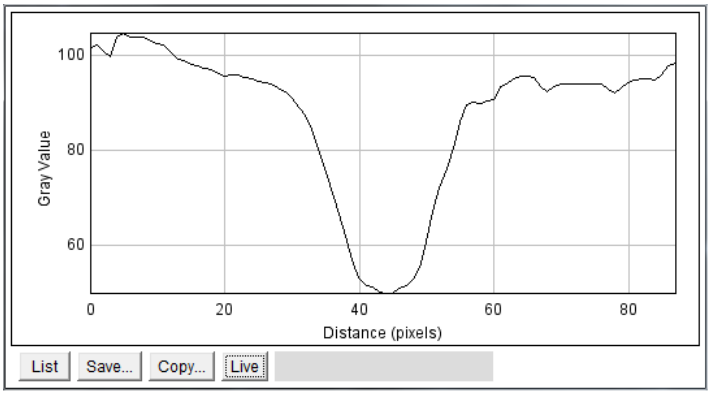

Figure 6.4: Gray value along the line depicted in Figure 6.3.

Taking into consideration the PMAG of 6 in the lens and the pixels size of 2.2 µm in the camera, the minimum resolvable object is calculated:

$$Image\ Spatial\ Resolution = \frac{1}{2 * pixel\ size} = 227.27\ \text{px/mm}$$

$$Object\ Spatial\ Resolution = ISR * PMAG = 1363.64\ \text{px/mm} \rightarrow 0.733 \mu m/px$$

Empirically, a flank of 15 pixels is calculated on the interface between two different objects. So the flank in micrometers is $0.733 * 15 = 11 \mu m$.

No objects smaller than this distance can be distinguished with this optical system.

6.3 DIC error estimation

The DIC code correlates by computing the normalized cross-correlation coefficient C, for a range of theoretical displacements (u', v') in 1 pixel increments by convolving the subset from the deformed image with the larger subset of the original image:

$$C(u',v') = \frac{\sum_{x',y'}\left[\left(r(x',y') - \bar{r}_{u',v'}\right)\left(d(x'-u',y'-v') - \bar{d}\right)\right]}{\left\{\sum_{x',y'}\left[\left(r(x',y') - \bar{r}_{u',v'}\right)^2\right]\sum_{x',y'}\left[\left(d(x'-u',y'-v') - \bar{d}\right)^2\right]\right\}^{1/2}}$$

Where x' and y' are the horizontal and vertical position of the subset and u' and v' are the horizontal and vertical displacements of the subset on the current test.

The equation that defines the maximum displacement u_{max} which the code is able to correlate successfully is:

$$u_{max} = \frac{SS}{2}(SZ - 1) - 1$$

The maximum displacement depends on two different parameters, the Subset Size (SS) and the Search Zone (SZ).

The choice of an appropriated Subset Size depends both on the observed surface and the optical system. It should thus be determined empirically on a case by case basis. Anyhow the Subset Size must be an even number to give a natural number as maximum displacement regarding the formula used by the DIC code.

The Search Zone is a value used to calculate the maximum displacement in which the program expects to find the element in the correlated picture. By default, the value of this parameter is 2, giving a maximum displacement of half of the Subset Size minus one. If the displacement is known to be bigger, one can modify either the Subset Size or the search zone to correlate de displacement. However increasing the Subset Size has its counterparts as it is shown in this chapter, therefore it can be useful to modify the Search Zone once determined the optimal Subset Size. Increasing either of these values increases the correlation time as well.

The error is calculated for several different Subset Sizes in every case:

$$\varepsilon = \sum_{p=0}^{N} \frac{|u_p - u_p^0|}{N}$$

Where:

- u_p is the horizontal correlated displacement for element p
- u_p^0 is the horizontal reference displacement for element p
- $N$is the total number of elements

To calculate the average error, the elements are not subtracted one by one, but the displacement matrixes are calculated and subtracted, as can be seen in Figure 6.5: Process for DIC error calculation. Then the average error is calculated

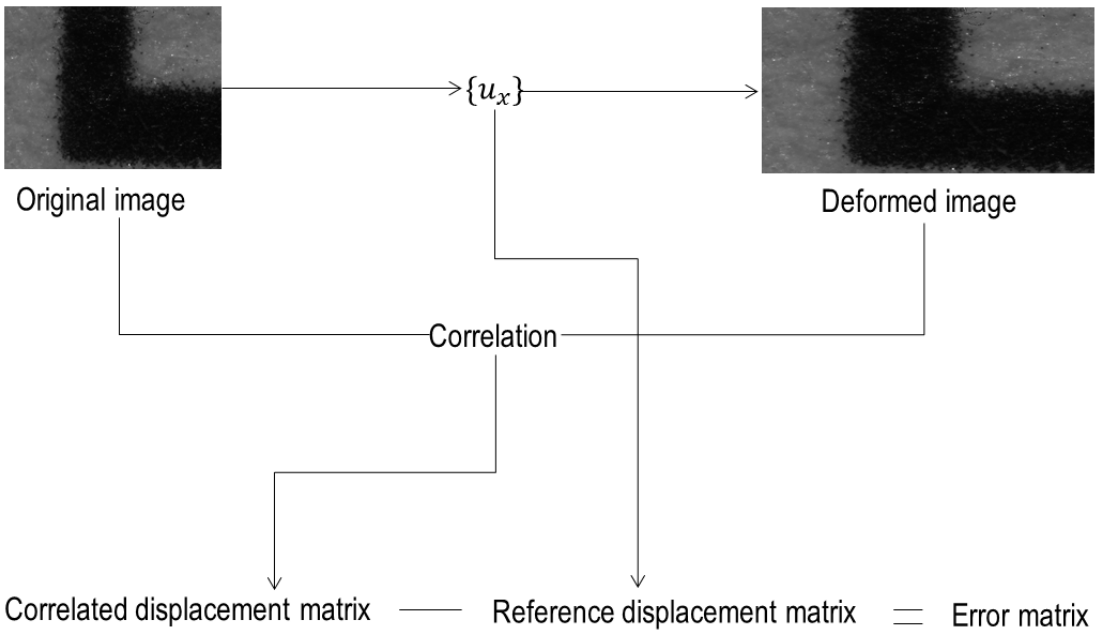

Figure 6.5: Process for DIC error calculation.

6.3.1 Error on a 1 pixel translation {u_x=1}

Each picture shows the result of the correlation for a 1 pixel horizontal displacement. As the Subset Size is increased, the deviation of the displacement values is reduced.

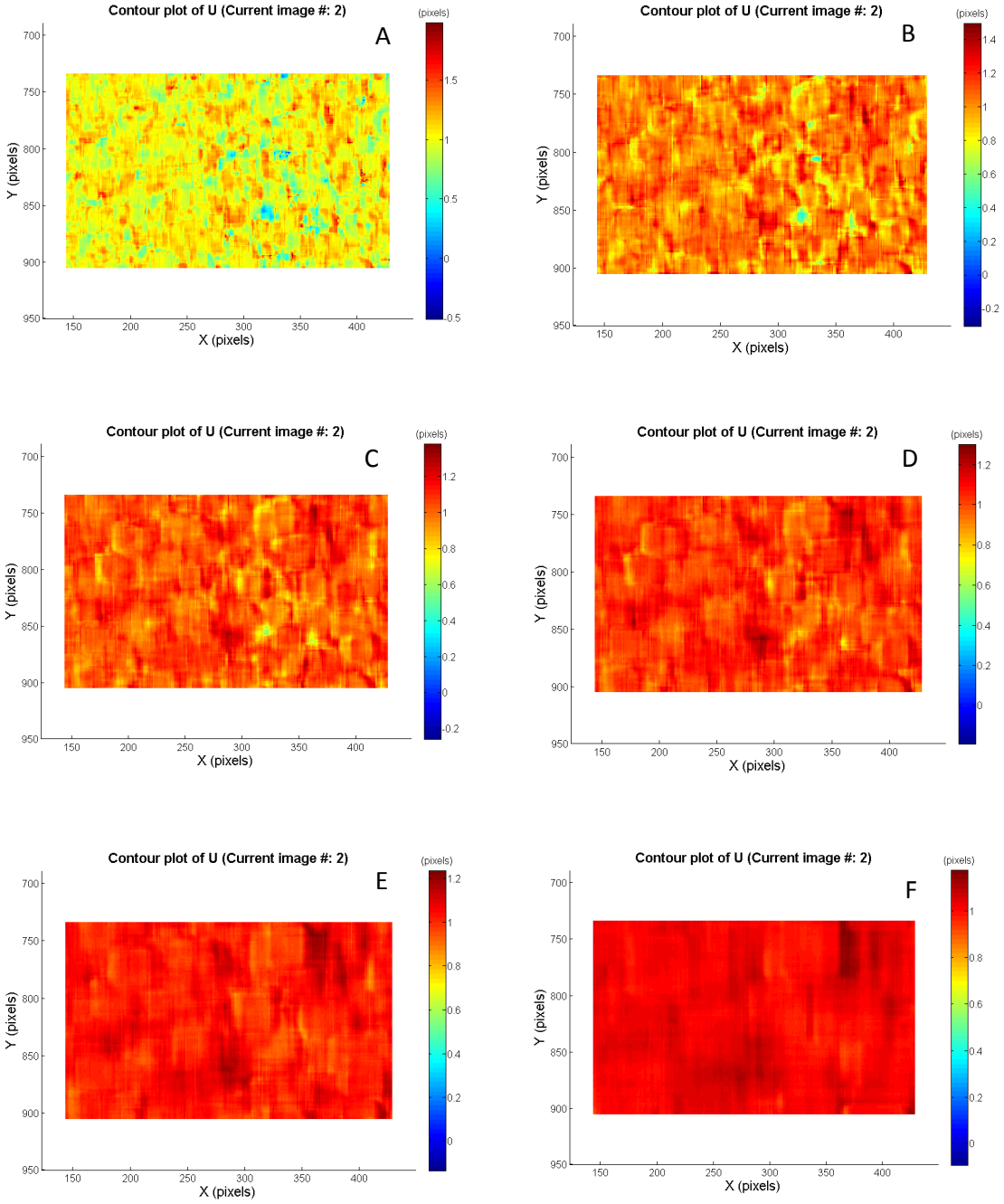

Figure 6.6: Translation contour plot with 10px, 14px, 18px, 22px, 30px, 50px Subset Size for figures A, B, C, D, E and F respectively.

The error is calculated subtracting a value of 1 pixel for every the whole x-displacement matrix. As expected from the contour plots, the average error is reduced while the Subset Size increases.

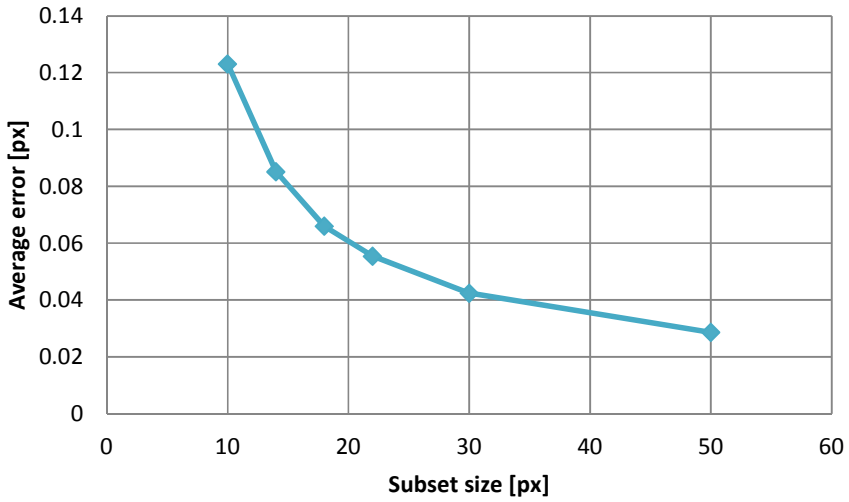

Figure 6.7: Average error for 1 pixel translation using different Subset Sizes.

6.3.2 Error on a 1 pixel horizontal flaw {u_x=1; Y≤152}

In this case the horizontal displacement is applied only to the upper part of the picture, the first 152 pixel rows, and the discontinuity surrounding area is correlated to check the error.

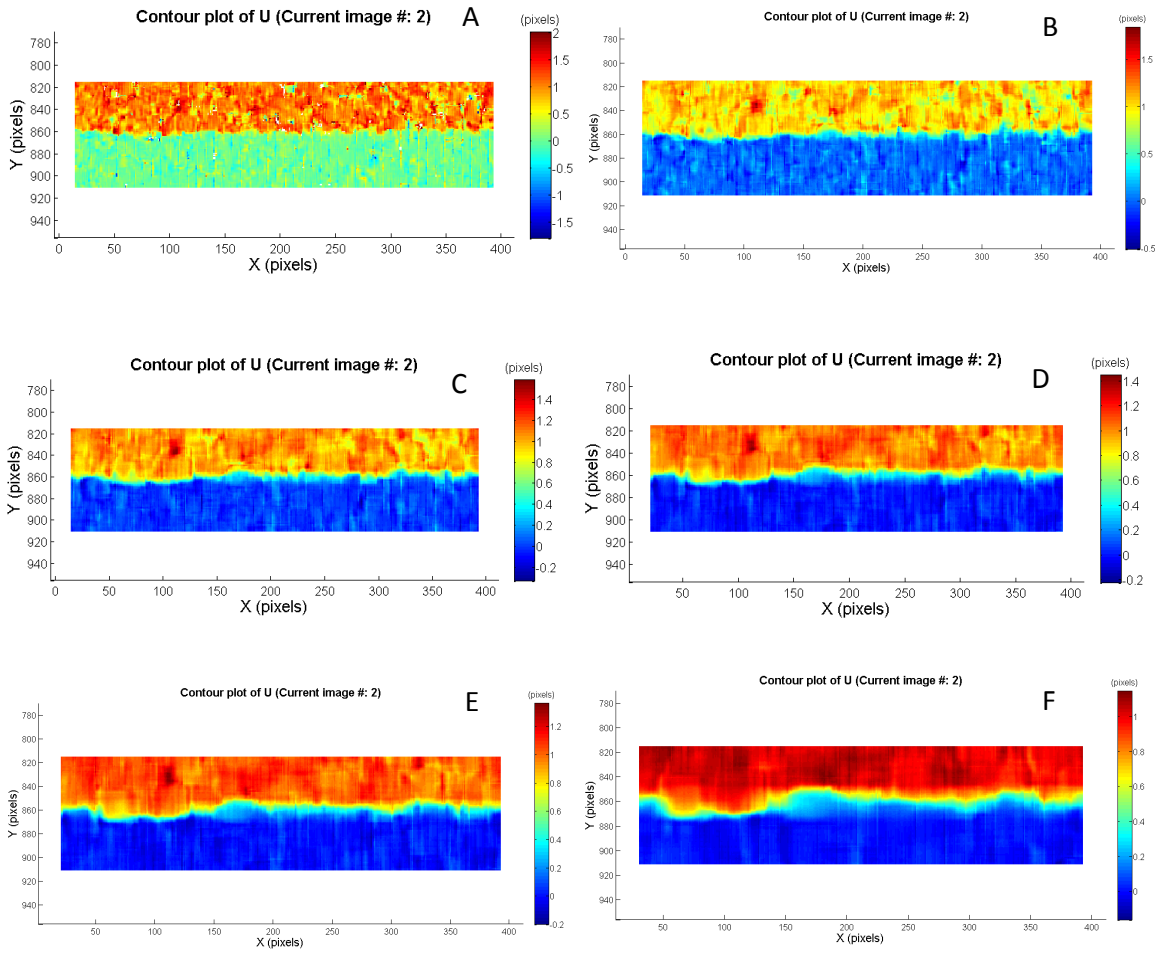

Figure 6.8: Flaw contour plot with 6px, 10px, 14px, 18px, 20px, 30px Subset Size for A, B, C, D, E and F respectively.

The plots show the same smoothing effect of the last case, so the error would be expected to reduce in the same way. However this case reveals how using a bigger subset makes the discontinuity line wider.

Plotting the average horizontal displacement of every row of pixels by every row reveals how using a bigger Subset Size reduces the resolution of the correlation.

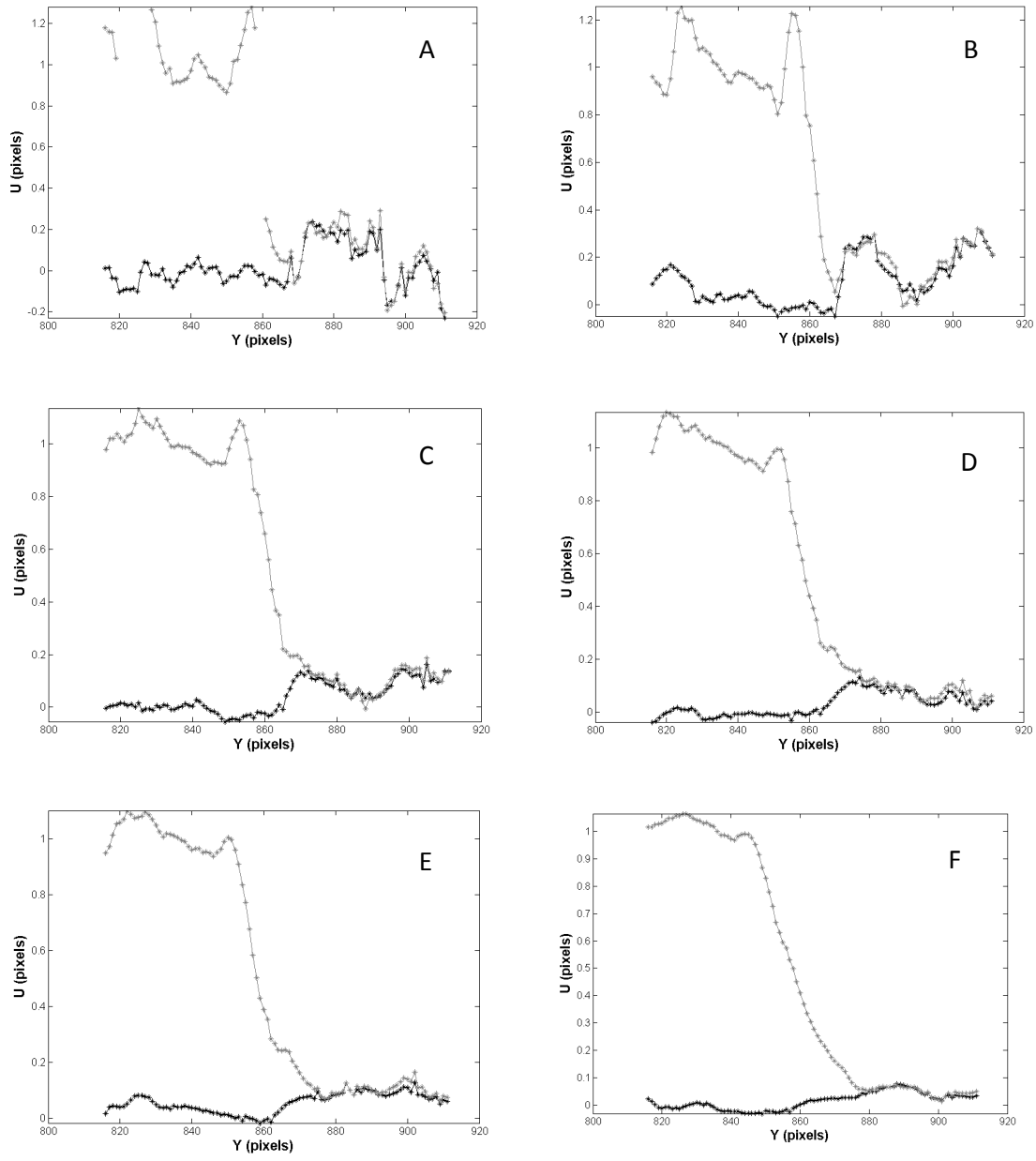

Figure 6.9: Horizontal average displacement for every row with 6px, 10px, 14px, 18px, 20px, 30px Subset Size for figures A, B, C, D, E and F respectively.

The error is calculated subtracting 1 from the first 152 rows in the x-displacement matrix.

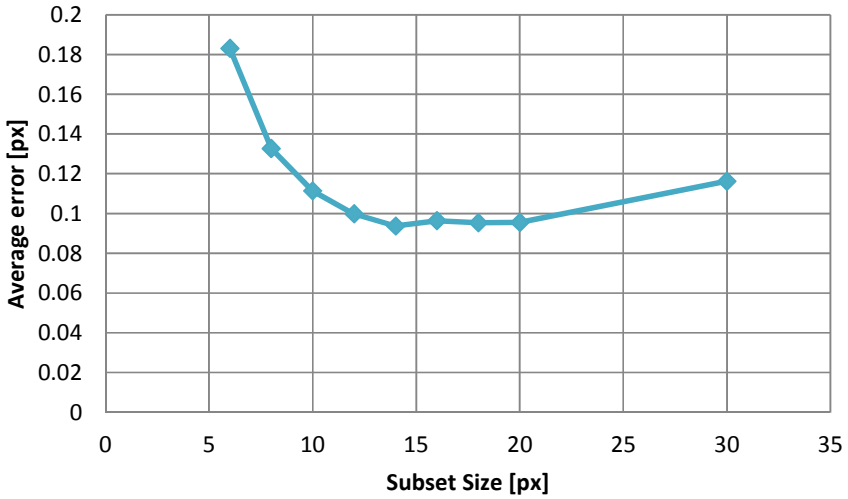

Figure 6.10: Average error for flaw using different Subset Sizes.

In this case there is a minimal error for at 14px. This means that the smoothing effect of a bigger Subset Size is compensated by the diffusion of the displacement lines.

6.3.3 Error on a linear deformation {u_x=0.09x}

The deformation applied to the picture in this case is a linear horizontal deformation. A horizontal zoom of is applied from the left side of the picture. The horizontal dimension is amplified to 1.1 times its previous size while the vertical dimension remains the same.

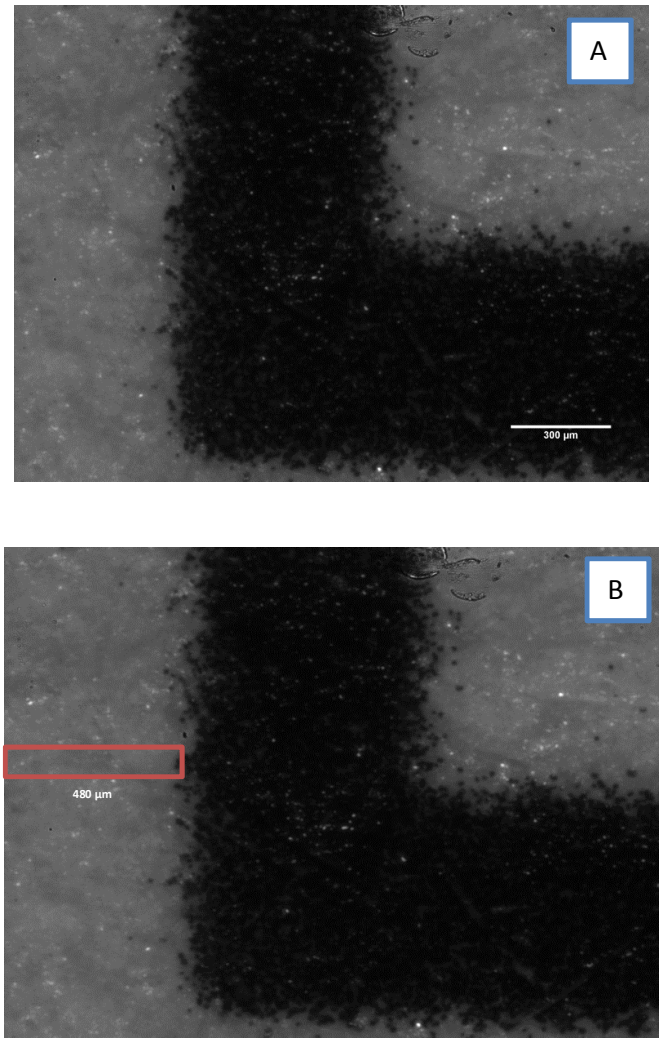

Figure 6.11: Original (A) and linearly deformed (B) target images. The area inside the red rectangle has been correlated.

In a first try, a Subset Size of 14 is chosen as it revealed to be optimal in the previous test.

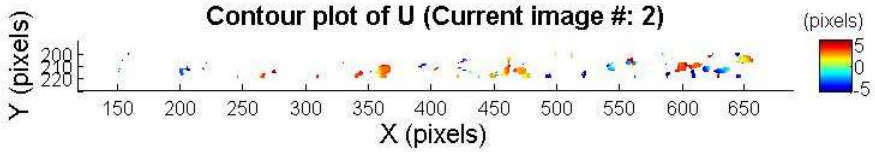

Figure 6.12: Contour plot for a linear deformation with a Subset Size of 14 pixel and Search Zone of 2.

The code is unable to find the element in the deformed image because the displacement values are higher than the maximum displacement allowed by the SS and the SZ.

To calculate the maximum displacement in this image we will need to know the position of the original picture in the new one. The resolution of our original picture is 2592x1944.

$$number\ of\ pixel\ columns * amplification = 2592 * 1{,}1 = 2851{,}2$$

$$2851{,}2 - 2592 = 259{,}2 \rightarrow \frac{259{,}2}{2851} = 0.\widehat{09}$$

The displacement of every pixel is $0.\widehat{09}$ times its original x position as calculated in the previous equation. The width of our correlating area is approximately 700 pixels. As initial correlation, 14 pixels is used for the subset size as it had the minimal error in the previous test. Using the formula of the maximum displacement depending on the subset size and the search zone, the optimal search zone value can be estimated.

$$700 * 0.\widehat{09} = \frac{14}{2}(SZ - 1) - 1 \rightarrow SZ = 10.233766$$

The same process is used to calculate the optimal search zone for every subset size in Table 6.1.

SS	30	20	18	16	14	12	10	8
SZ	5.3091	7.4336	8.1818	9.0795	10.2337	11.7727	13.9273	17.7727

Table 6.1: Search Zones for different Subset Sizes.

In all cases the image is fully correlated with no missing information:

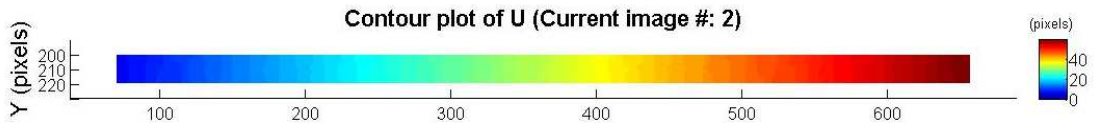

Figure 6.13: Contour plot for linear horizontal deformation for 8px, 10px, 12px, 14px 16px, 18px, 20px and 30px Subset Size.

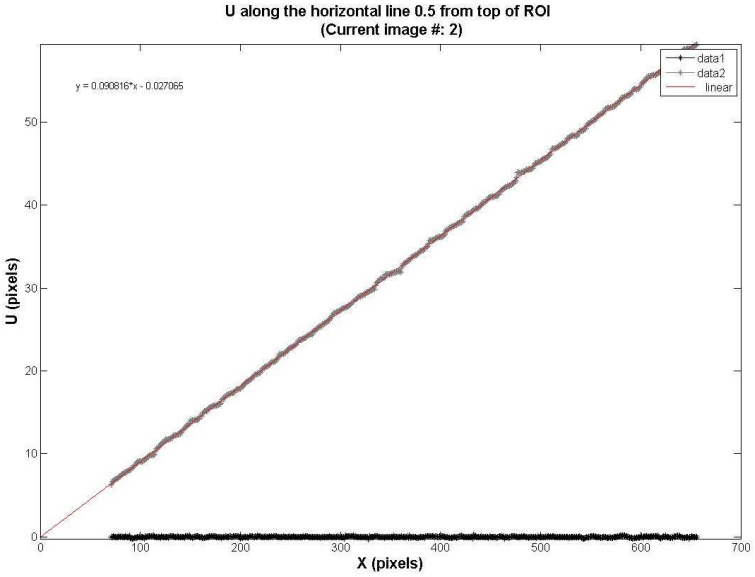

Figure 6.14: Linear plot of the displacement for 8px, 10px, 12px, 14px, 16px, 18px, 20px and 30px Subset Size.

To calculate the error in this test the known slope is used to subtract a reference slope from the data correlated.

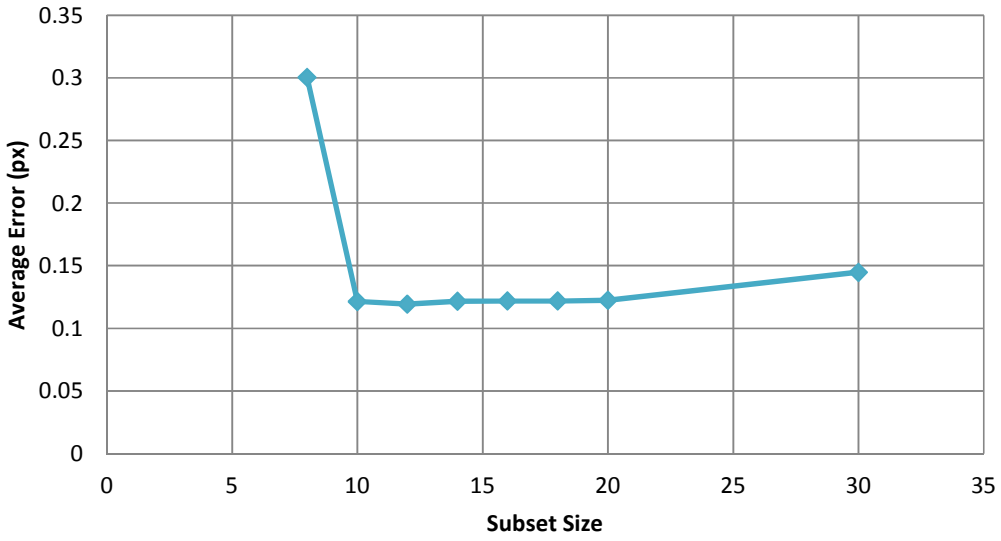

Figure 6.15: Average error with linear deformation for different values of Subset Size.

The minimum error is in this case 12px. The experimental results give an estimation of an optimum value of 12-14px for the Subset Size.

6.4 Experimental procedure

The aim of this project is the study of the mechanical properties of the fuel cladding material taking in consideration the effects of hydrogen uptake during the irradiation cycles. However no irradiated cladding is used during the tests; working with real irradiated cladding would include additional complexity to the project. Therefore, it is necessary to use hydrogenation devices, among others, to prepare the samples before starting the mechanical testing.

Only thermal experiments have been conducted during this study. However thermo-mechanical essays would follow a similar procedure, with added complexity. Figure 6.1 shows the position of the camera and the light cold source used during an early test.

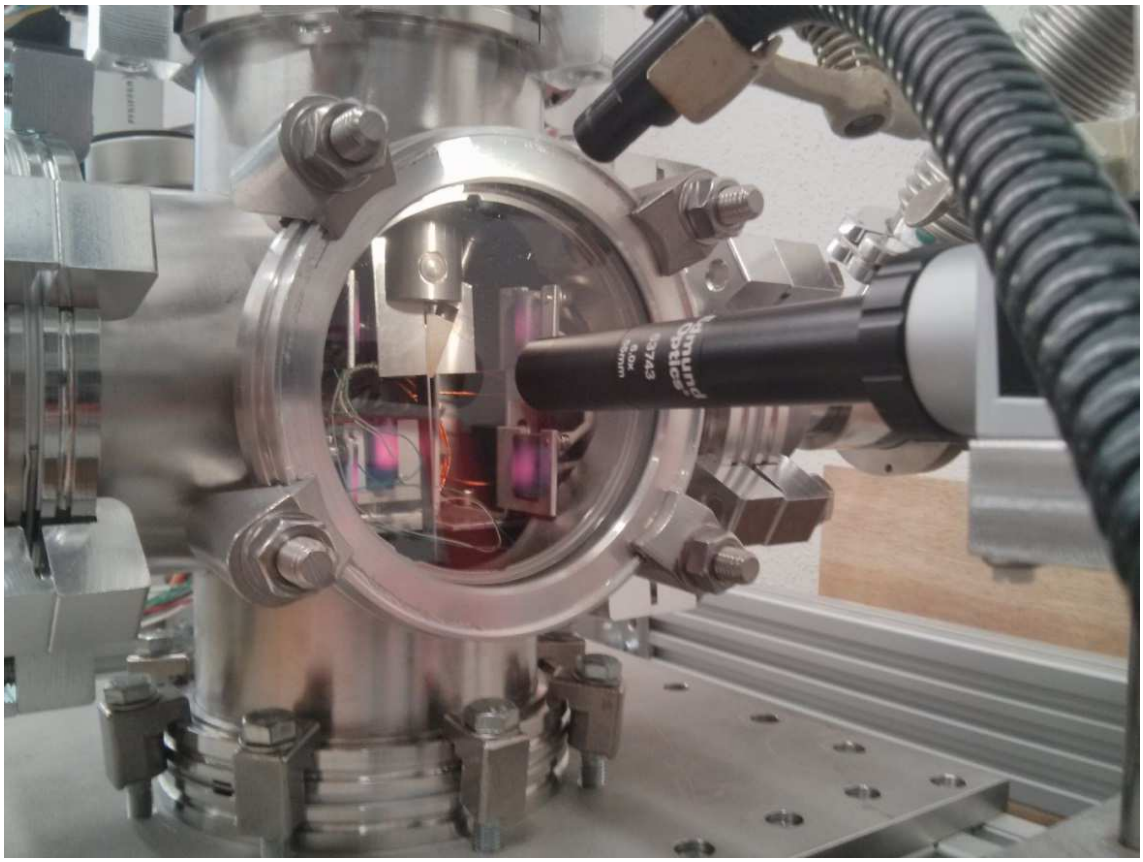

Figure 6.16: Example of a thermal test.

6.4.1 Hydrogenation

Zircaloy samples are hydrogenated in an oxygen-free atmosphere inside a furnace for several days. Once vacuum is created inside the glass where the sample is placed, hydrogen is allowed to enter and the hydrogenation begins. The samples are sheets of Zry-2 and Zry-4 with a thickness of 0.6 mm thickness and diverse length and width.

Figure 6.17: Sample of Zircaloy (left) and hydrogenation furnace (right).

6.4.2 Polishing

After hydrogenation, the 0.6 mm surface is polished. The procedure begins with a careful cleaning of the whole piece with acetone and further rinsing. Using a standard polishing machine, the scope surface is treated progressively with smaller grain size up to P 2500. The polishing process, if properly performed, creates a surface which is usable for DIC.

The criteria to know if a picture is good for correlation are:

- No saturated pixels, i.e. no extreme whites or blacks in the picture
- Surface pattern with a similar order of magnitude over the scope surface
- The whole correlation surface must be focused
    - The surface must be perpendicular to the camera
    - The surface must be as finely polished as possible

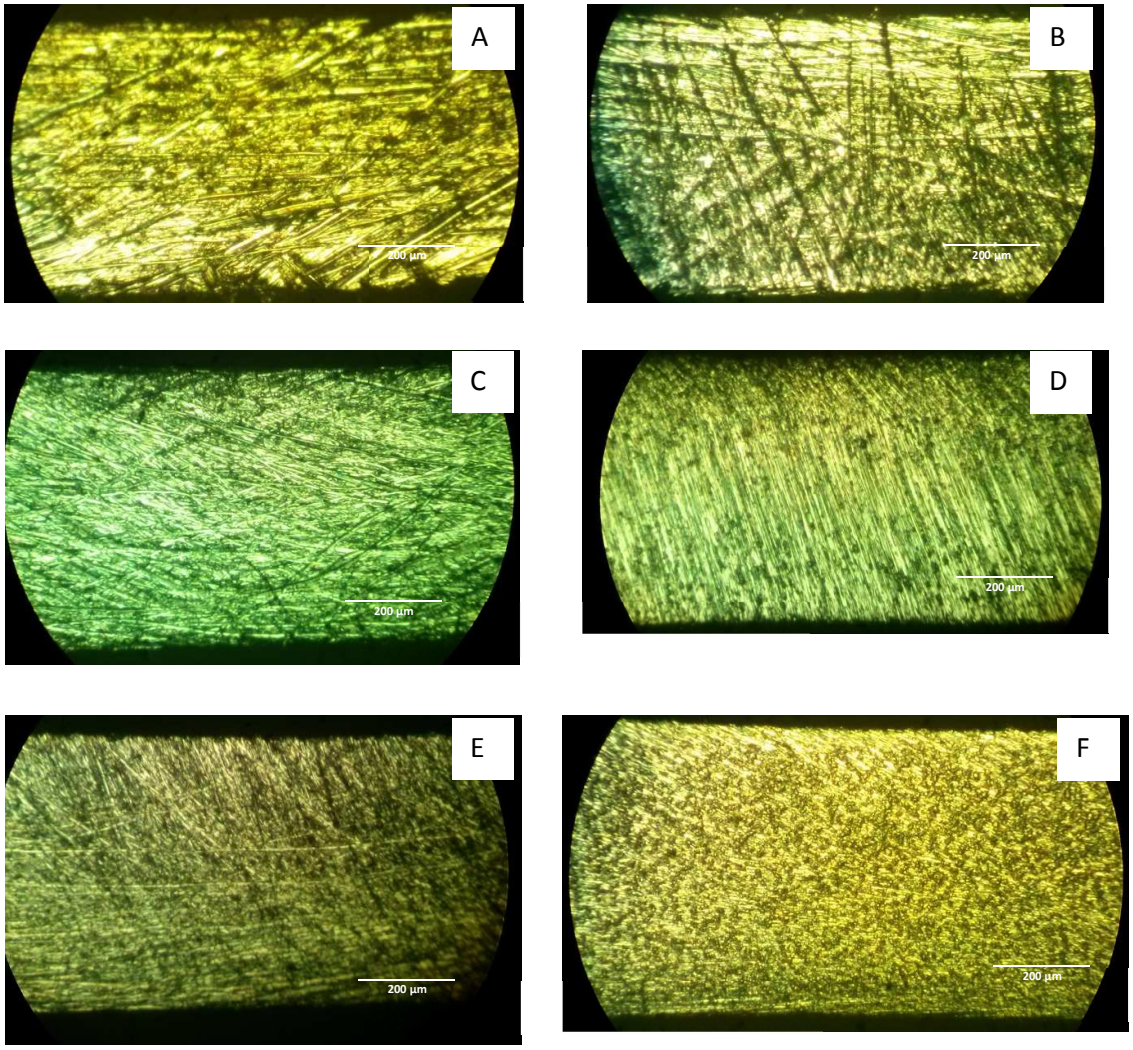

Figure 6.18: Zircaloy simple after being polished with 80p, 180p, 320p, 400p, 500p and 1200p grain size sandpaper for A, B, C, D, E and F respectively.

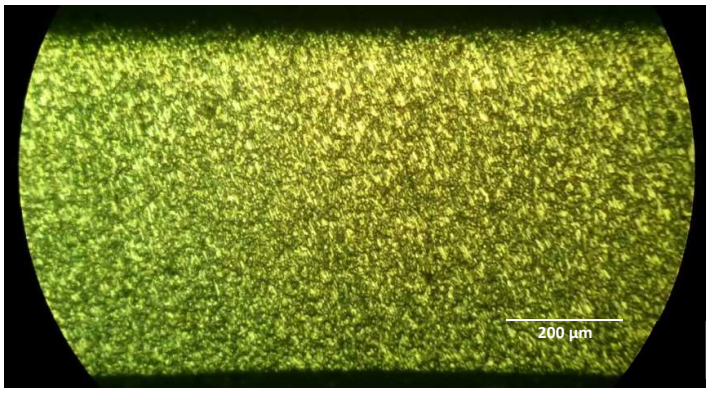

Figure 6.19: Zircaloy simple after final polishing with 2500p grain size sandpaper.

Once the sample is polished, it is analysed with a microscope to check if the surface is ready for correlation. The surface must be as smooth and flat as possible.

With a fine polishing the conditions needed for a good correlation are often achieved without further procedures. However the scoop surface can be sprayed with black paint to provide the image correlation software with a map to follow the displacements on the surface of the sample.

6.4.3 Sample set up

The sample holders must be clamped to the extremes of the piece, and the 3-piece set up is introduced inside the 6-way cross cell. When the sample with the holders is fixed to the pulling rods in the cell, the thermocouples must be placed in the surface of the sample. For this purpose, six holes are drilled on every sample holder.

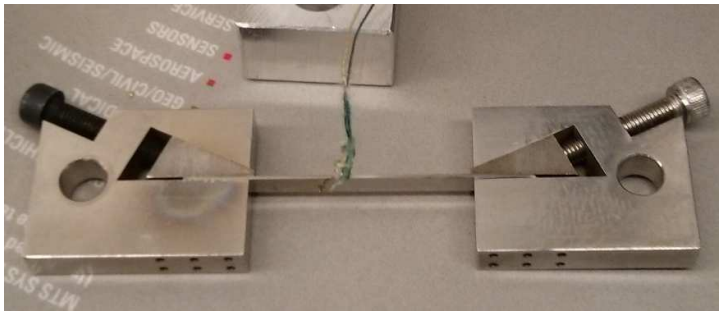

Figure 6.20: Sample placed in the simple holder with a welded thermocouple.

The thermocouples can be easily introduced inside each one of them and effectively measure the temperature in the surface of the sample. One of the thermocouples is directly welded to the sample. The sample must be perpendicular to the camera before placing the window flange.

Once closed, the camera must be oriented to focus the sample. The image acquisition is carried on by the pylon Viewer 64-bit of BASLER. The configuration is set usually with a low exposure time and direct light. Then It is safe to heat up the sample to the desired temperature with no risk of superficial changes due to oxidation. After that, the force is applied to the sample, and the procedure is recorded by the DIC camera for future correlation.

6.5 Estimation of the LTE coefficient of non-hydrogenated Zircaloy-4

The LTE coefficient has been estimated as a way of validating the machine. A sheet of non-hydrogenated Zircaloy-4 is the target for this experiment.

The parameters for this correlation are shown in Table 7.1.

Subset Size [px]	Search Zone	Distance between elements [px]	Min. Temperature	Max. Temperature	Number of pictures
18	3	5	26.11	132.52	12

Table 6.2: Correlation parameters.

The distance between elements has been increased to 5 px from the calibration experiments to limit the correlation time. However no displacement on this order of magnitude is expected on a thermal experiment. Figure 7.1 shows the area correlated:

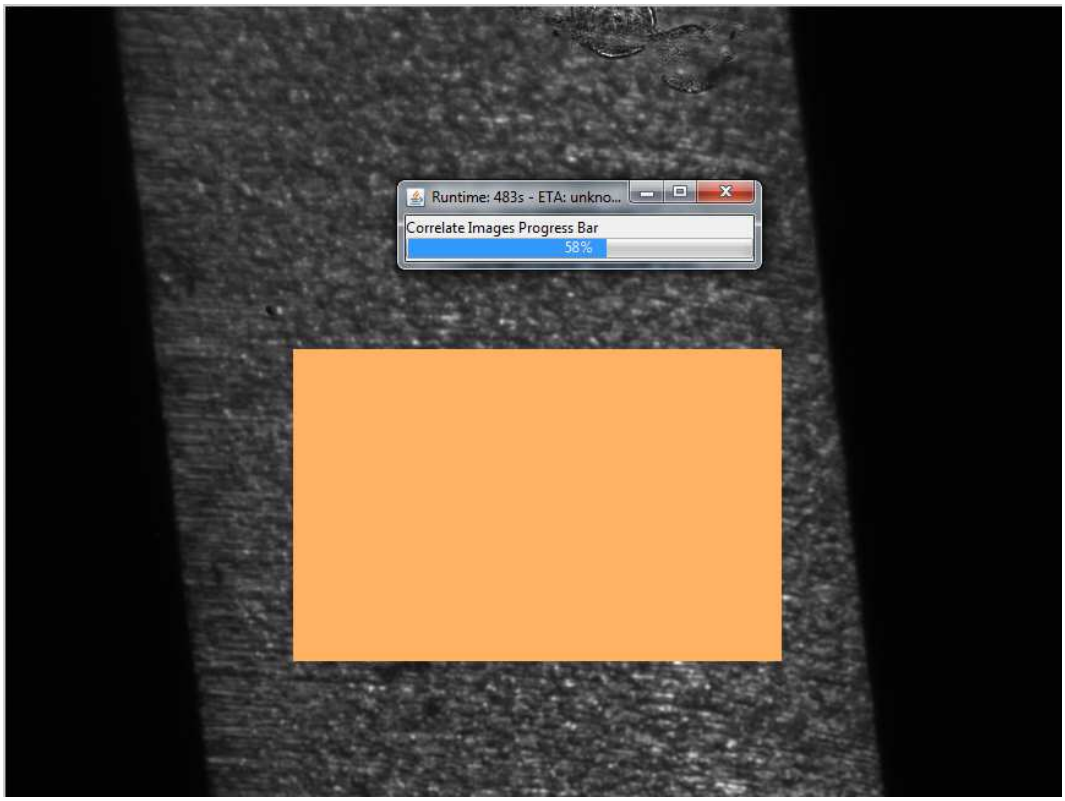

Figure 6.21: Grid shown over the correlated area. The time of correlation is not negligible.

After the correlation, the rigid body displacement has to be removed from the data, so that deformation can be analysed. To do this, the first element of the correlation is chosen as an origin of coordinates, and its vertical and horizontal displacement are blocked. The displacement value of this element is subtracted from all the elements for every picture.

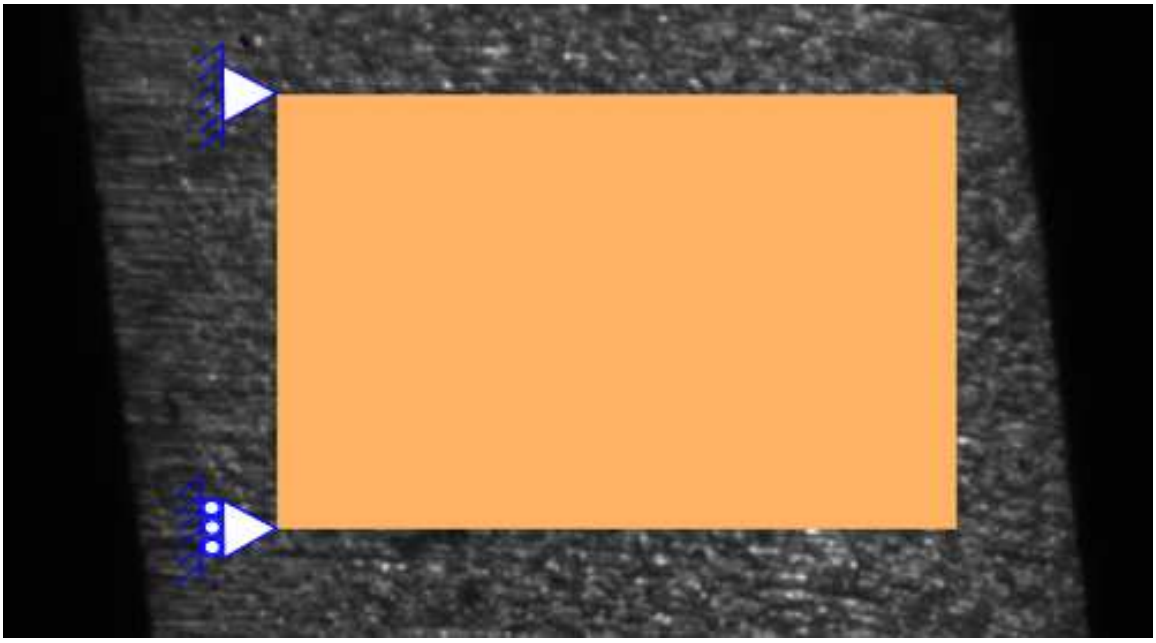

Figure 6.22: Movements blocked to remove the rigid body displacement.

After removing the vertical and horizontal displacements, the solid rotation has to be removed from the displacement field too. Therefore a second point has to be blocked, as shown in Figure 7.2. The value of the horizontal displacement in point B is divided by the vertical position to obtain the omega of the sample (centred in the origin of coordinates). The solid rotation displacement of every point is calculated with this omega and subtracted from all the elements in the sample.

This process eliminates all displacement in the vertical and horizontal directions as well as the rigid body rotation, and is required due to the vibrations and relative movement between the camera and the sample during the test.

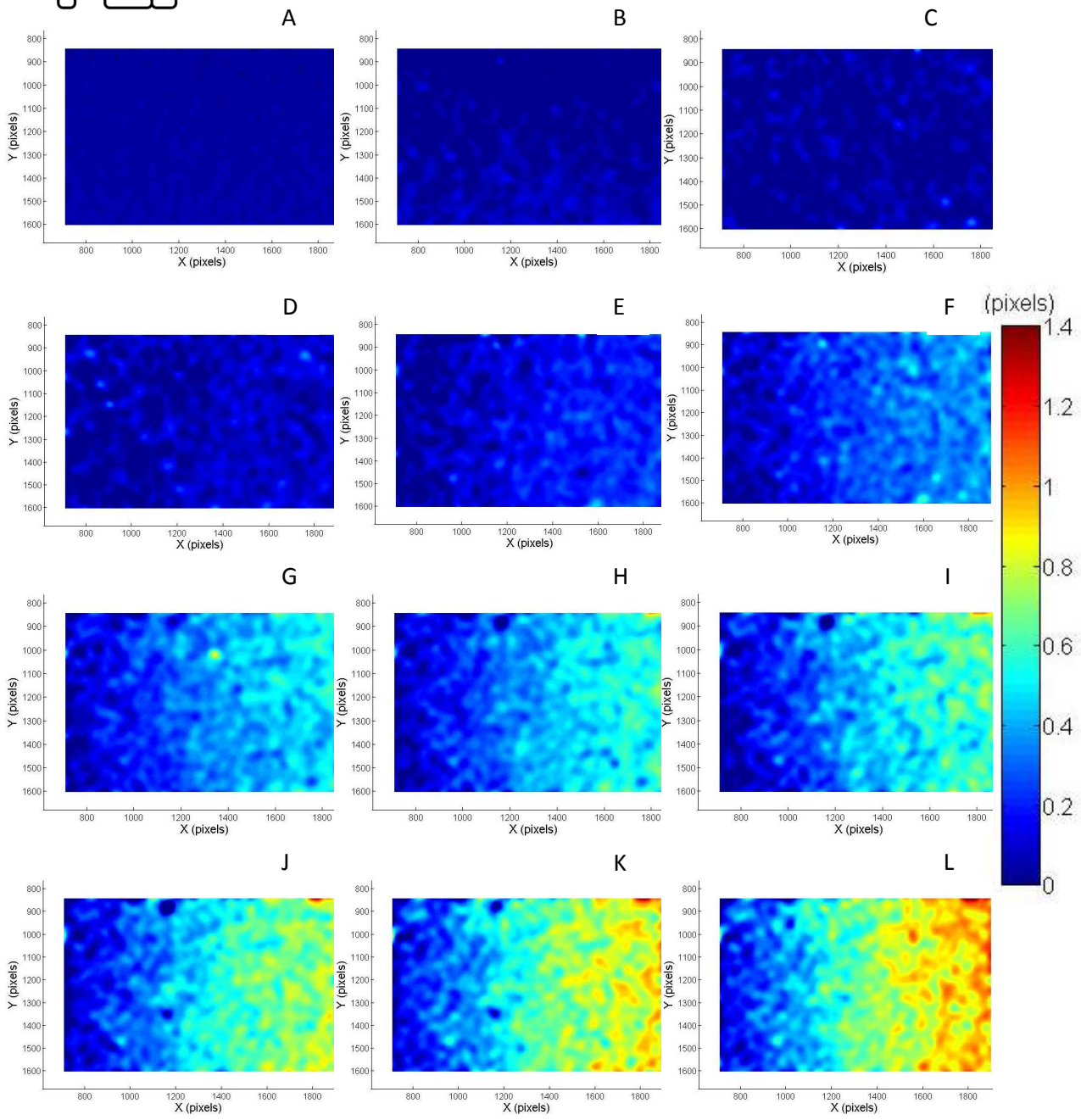

Figure 6.23: Contour plot of the horizontal thermal expansion for non-hydrogenated Zr-4. Pictures A, B, C, D, E, F, G, H, I, J, K and L correspond to temperatures of 26.11, 25.86, 26.26, 35.45, 47.67, 60.07, 72. 95, 85.26, 97.68, 109.42, 121.31, 132.52 ºC.

Figure 7.3 shows the horizontal displacement of the elements of the sample once removed the rigid body motion. The correlation between temperature and expansion is clear.

Plotting the value of the average horizontal displacement for every temperature Figure 7.4 is obtained.

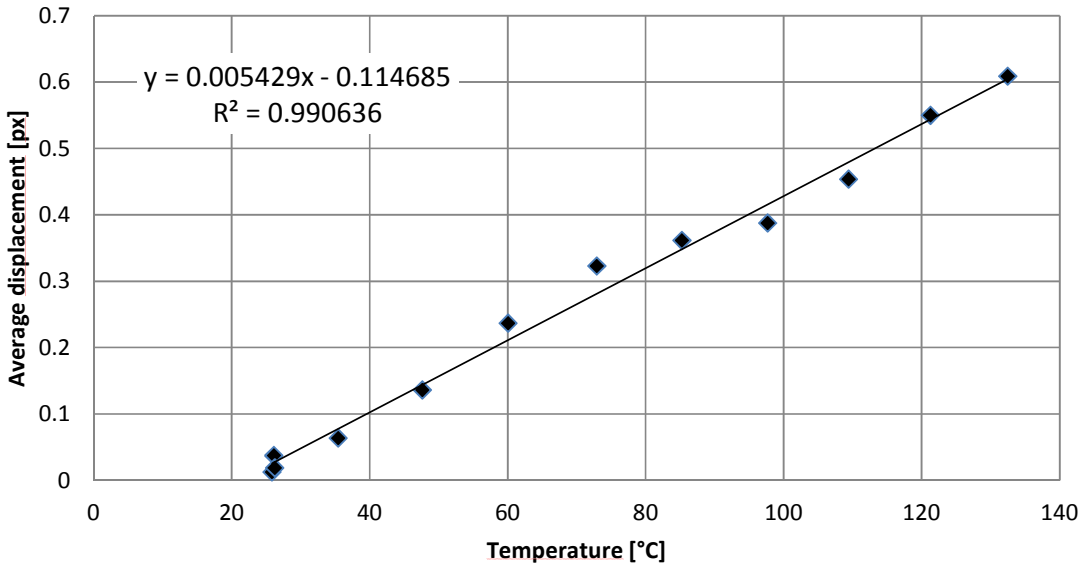

Figure 6.24: Curve of thermal expansion of Zircaloy-4.

The displacement field assumed for a thermal expansion is

$$\underline{u} = \left(\propto_x x\underline{e}_x + \propto_y y\underline{e}_y\right) * \Delta T$$

Then, the average displacement, by definition, is calculated

$$\overline{\underline{u}} = \frac{\Delta T}{L_x L_y}\int_{y=0}^{L_y}\int_{x=0}^{Lx}\underline{u}dxdy = \frac{\Delta T}{L_x L_y}\left[\propto_x \left[\frac{x^2}{2}L_y\right]_0^{L_x}\underline{e}_x + \propto_y \left[\frac{y^2}{2}L_x\right]_0^{L_y}\underline{e}_y\right] =$$

$$= (\propto_x \frac{L_x}{2}\underline{e}_x + \propto_y \frac{L_y}{2}\underline{e}_y)\Delta T$$

Taking the value of slope from Figure 7.4, the expansion in the horizontal direction is:

$$\propto_x = \frac{2}{L_x}\frac{\overline{u}}{\Delta T}\underline{e}_x = \frac{2}{5 * 238} * 0.005429 = \mathbf{9.12437 * 10^{-6}{}^{\circ}C^{-1}}$$

Lx is the length of the horizontal dimension, and it is equal to the number of elements in the horizontal direction (238) multiplied by the size of every element (5px). Literature gives a LTE coefficient between $5.8 * 10^{-6}$ and $6 * 10^{-6}{}^{\circ}C^{-1}$.

The linearity is clear and the value of LTE coefficient is in the same order of magnitude than the theoretical value. Suggestions to improve this measure are explained in the future work.

7 Budget

7.1 Labor costs

The work costs include all the money spent in the student during the nine months of work. The first period comprehends the first six months, from September to February. During this time the student has been paid a master's student salary from PSI. Along with this salary, the student has been receiving an ERASMUS scholarship during this period. The other expense included in the calculations is the 3-day training course in LabView Core 1 that I have has completed during October 2013.

Reason	Cost per month [CHF/month]	Months	Cost (CHF)
Master's Student Salary	600	6	3600
Trainee Salary	2100	3	6300
LabView Course			1549
Total salary			**11449 CHF (9404.13€)**

Table 7.1: Salary and training expenses paid by PSI during the project.

The second period comprehends the next three months, from the beginning of March to the end of May. The student was paid occupying a trainee position at PSI. No further allowance was paid by the ERASMUS programme.

Reason	Cost per month (CHF/month)	Months	Cost (CHF)
ERASMUS scholarship	274	6	1644
Total scholarship			**1644 CHF (1350.44 €)**

Table 7.2: Scholarship costs paid by UPC during the project.

7.2 Equipment costs

Provider	Reference	Product description	Qty.	Price [CHF]	Subtotal [CHF]
HBM	1-U9B/2kN	load cell / 2 kN	1	753.00	
					753.00
Cedrat	APA	Piezo-electric actuator	1	2976.00	
	CA45	Actuator controller	1	1116.00	
					4092.00
Rose+Krieger	7216011-0100	Guiding linear unit EP 60	1	700.20	
	90906	Handrad	1	56.50	
					756.70
	Total force system				**6343.38 CHF (5210.41 €)**

Table 7.3: Cost of the components that form the force system of the machine.

Provider	Reference	Product description	Qty.	Price [CHF]	Subtotal [CHF]
Abecon	MSH/20	Infrared heating diode with thermocouple	6	361.80	
					361.80
Radiospares	6EP13532BA00	Siemens, controllable power supply	3	618.66	
	428-477	Netzteil DIN-Schiene 24VDC 2,5A	1	92.83	
		Various	1	30.19	
					741.68
	Total heating system				**1103.48 CHF (906.39 €)**

.

Table 7.4: Cost of the components that form the heating system of the machine.

Provider	Reference	Product description	Qty.	Price [CHF]	Subtotal [CHF]
Pfeiffer		HiCube 80 Eco, DN 40 ISO-KF, MVP 015	1	5500.00	
		DN63ISO-K to DN40ISO-KF adapter	1	61.00	
					5561.00
Hositrad	ISOX6/100	ISO-K 6-way cross ISO-K 100	1	948.60	
	ISO100/102	ISO-K weld flange ISO-K 100 / SST304 / D 101.6	1	36.83	
	ISO100B	ISO-K blank flange Flange ISO-K 100	4	147.31	
	ISO100/40A	ISO-K to KF adaptor ISO-K 100 to NW40Kf	2	133.92	
	HVP-ISO100	ISO-K viewport zerolength glass	1	217.62	
	CC25KF	NW25KF clamping collar	1	39.06	
	CC40KF	NW40KF clamping collar	3	133.92	
	KF25/FC	KF face clamp NW20KF and NW25 KF flange	2	62.50	
	KF25/BS25	NW25KF blank stub stainless steel 304	3	40.18	
	VAV40KF	Manually operated valve	1	329.22	
	13744-02-KF	NW40KF 20 pins connector	1	599.29	
	18618-02-KF	NW16KF 3 pairs thermocouple feedthrough	1	370.51	
	KTR40/16	KF Reducer tee 40-16	1	45.20	
	ISO63/CG304	ISO-K single wall clamp	10	44.08	
	ISO63C/SS	ISO-K double claw clamp	6	40.18	
	ISO63CA	ISO-K double claw clamp	34	66.40	
	ISO100SV	ISO-K centering ring flange ISO-K 10 / material SST304	6	120.53	
	KF25/R	KF centering ring flange NW25KF / mat. SST304	4	13.39	
	KF40/R	KF centering ring flange NW40KF / mat. SST304	4	17.86	
	KF16/R	KF centering ring flange NW16KF / mat. SST304	2	5.02	
	21643-01-A	In-Vacuum cable kapton	1	63.61	
					3411.61
BRW		Spring	10	64.70	
					64.70
Mewasa		KF weld edge bellow, DN25/64mm/37mm/75mm	1	438.00	
					438.00
		Total vacuum system		**9475.31 CHF (7 782.95 €)**	

Table 7.6: Cost of the components that form the optical system of the machine

Table 7.5: Cost of the components that form the vacuum system of the machine.

Provider	Refe-rence	Product description	Qty.	Price [CHF]	Subtotal [CHF]
Edmund Optics	63-743	6x tech-spec telecentric lenses, 65mm WD	1	700.91	
	88-325	Basler ACE acA2500-14um mono-chrome usb camera	1	818.71	
	55-177	50/PK S.H.C.S. #1/4-20x3/4IN	1	15.31	
	36-481	3.0" Medium Mirror Mount	1	123.07	
	55-020	Large X-Y Axis Leadscrew Drive	1	399.34	
		Total optical system			**2057.35 CHF (1689.89 €)**

Table 7.6: Cost of the components that form the optical system of the machine.

Provider	Reference	Product description	Qty.	Price [CHF]	Subtotal [CHF]
NI					
	779001-01	NI 9211 4-Ch ±80 mV, 14 S/s, 24-Bit TC and Diff AI	1	387.00	
	779017-01	NI 9932 Backshell with 10-pos con-nector block (qty 1)	1	39.00	
	779781-01	NI 9219 4 Ch-Ch Isolated, 24-bit, ±60V, 100S/s Univeral AI Module	1	1170.00	
	196720-01	NI 9972 Backshell for 6-pos con-nector block (qty 4)	1	39.00	
	779012-01	NI 9263 4 ch,16-bit, +/-10 V, 100 kS/s/Ch, AO Module	1	445.50	
	781157-01	cDAQ-9174, CompactDAQ chassis (4 slot USB)	1	805.50	
	763065-01	Power Cord, 220V, 10A, Swiss	1	12.00	
		freight	1	28.26	
					2926.26
Fujitsu-Siemens		FSC Esprimo P910 (Core i5-3470)	1	1050.00	
					1050.00
		Total control system			**3976.26**

Table 7.7: Cost of the components that form the control system of the machine.

7.3 Total

Concept	Note	Cost [CHF]	Cost [€]
Salary		11449.00	9404.13
Scholarship		1644.00	1350.44
Equipment	Force system	6343.38	5210.41
	Heating system	1103.48	906.39
	Vacuum system	9475.31	7782.95
	Optical system	2057.35	1689.89
	Control system	3976.26	3266.07
	Subtotal	22955.78	18855.71
	Total	**36048.78**	**29610.28**

Table 7.8: Total budget of the Project detailed.

8 Environmental impact

The environmental impact of this prototype is explained as the power and energy consumed by all the components that integrate the machine, and the CO_2 emissions related to this consumption. In Table 8.1 the power consumption for every component is summarized and also added to calculate the maximum power the prototype can consume. The time column is an estimation of how many hours that component is used during an experiment performed with the prototype until results are ready.

The test takes place during 2 hours, but the vacuum pump is usually working from the day before to have proper vacuum. The 5 hours for the pc include the time of the test, correlation time and the data analysis.

Component	**Number**	**Consumption [W]**	**Time [h]**	**Energy [kWh]**
PC	1	280	5	1.4
Screen	1	78	5	0.39
Vacuum pump	1	230	22	5.06
Vacuum gauge	1	2	22	0.044
Radiator	6	330 (55 per unit)	2	0.66
Piezoelectric actuator	1	165.6	2	0.3312
Force gauge	1	1	2	0.002
cDAQ-9174	1	15	2	0.03
acA-2500 camera	1	2.2	2	0.0044
Lightbulb	1	36	2	0.072
Total		809.8		7.9936

Table 8.1: Power and energy consumption of the prototype.

Once known the power consumption, it is interesting to estimate the maximum equivalent CO_2 emissions and the average emission of one experiment. The electricity production in Switzerland is divided roughly between a 40% nuclear and 60% hydraulic. Regarding the emissions calculated for this sources by the International Panel for Climate Change[8]:

Technology	50^{th} percentile [gCO_{2eq}/kWh_e]	Energy production [%]
Hydroelectric	4	60
Nuclear	16	40

Table 8.2: Equivalent CO_2 emissions for hydroelectric and nuclear electricity.

The weighted mean of this value results in: 8.8 gCO_{2eq}/kWh_e

Which multiplied by the average energy consumption of a single experiment gives a value of

70.34 gCO_{2eq}/experiment

During the maximum power consumption, the emission per hour reaches:

7.13 gCO_{2eq}/hour

Conclusions

The first part of the project consisted on an extensive literature review on the process of hydrogen uptake and effects of hydrides on nuclear-grade zirconium. An accurate topic knowledge is essential to define the characteristics of a machine which is intended to study these effects. Further work on this prototype will allow observing this phenomenon.

The key dimensions of all the pieces of the machine were previously defined. An important part of the early work on this project has been dimensioning of the structural components of the machine using LibreCad. The frame has been drafted using SketchUp, ordered and built.

The LabView code has been developed to acquire the relevant data of the test and control the temperature with a PID controller. A LabView Core 1 course was taken as apprenticeship for this task. The hardware/software communication as well as the code optimization had required training completion from the National Instruments forums.

The electrical circuits of the heating system and disposition of the electric box have been specified and installed. The installation of the electric box, as well as out-vacuum and in-vacuum electrical systems have been possible only with the help of the technicians in the lab.

The vacuum system has been tested in ideal and experimental conditions. Expertise on the use of vacuum technology has been acquired to perform the setup and the operation of the in-vacuum components of the machine.

The optical system has been carefully installed, tested and characterised. The use of highly sensitive equipment in a working environment has required special care on the cleanliness.

The Digital Image Correlation technique has been analysed and characterised for the purpose of the prototype. ImageJ has been used for picture alteration and processing.

All the installed components of the prototype have been validated by estimating the linear thermal expansion coefficient of Zircaloy-4 using DIC.

Future work

- A redesign of the force system is necessary to place the force gauge outside the vacuum cell.
- A redesign of the tensile system is required for better homogeneity of temperature.
- The piezoelectric actuator has to be ordered and installed.
- An additional translation platform in the vertical direction for the optical system is recommended.
- Some vacuum tight pieces must be redesigned if higher vacuum is required.
- For DIC, the Parallel Computing Toolbox of Matlab could be useful to save time in large correlations.
- Using the PID and Fuzzy Logic Toolkit for LabView could simplify the PID parameters calculation and improve the temperature control.

Acknowledgments

I would like to thank in first place Dr Stéphane Valance for his guidance during the last 9 months. For trusting me in tasks I felt unachievable, for teaching me material science and for the extensive corrections for this and other papers.

At the same time I want to acknowledge Dr Ralph Spolenak from ETH for supervising this thesis and Dr Javier Dies from UPC for his tutorship and advice.

I feel grateful to Mr. Robert Zubler for his help in every part of the project. His heuristic knowledge for problem-solving has been indispensable.

As well I want to express my gratitude to Dr Johannes Bertsch for making possible my stay at PSI and for solving any bureaucratic issues I had during the past months.

I thank Dr Cyprian Mieszczynski, Dr Melanie Chollet, Dr Lyubomira Veleva, Dr Henar Rojo, Mr Ignasi Villacampa, Miss Anna dal Farra, Mr Daniel Ulloa, Mr Carlos Vigo, Mr Albert Riera and Mr Miquel Bonet for all the coffees and meals and talks we enjoyed together.

Thanks to Miss Regina Surber, Mr Renzo Iten, Mr Marc Hüppin and Mr Philippe Haensler for making me feel at home despite of the distance and the language barriers.

And finally thanks to my mother Isabel, my father Ricard, my sisters Chon, Isabel, Ana, Marta, Rut, Arán, my brothers Ricard, Pedro, Raúl y Carlos and my girlfriend Irene, for inspiring and supporting me always.

Bibliography

[1] G. D. Moan and P. Rudling, *Zirconium in the Nuclear Industry: Thirteenth International Symposium*. .

[2] H. Okamoto, "H-Zr (Hydrogen-Zirconium)," *J. Phase Equilibria Diffus.*, vol. 27, no. 5, pp. 548–549, Oct. 2006.

[3] J. Blomqvist, J. Olofsson, A.-M. Alvarez, and C. Bjerkén, "Structure and thermodynamical properties of zirconium hydrides from first-principle," 2011, vol. 1, pp. 635–643.

[4] S. Ells, C. E. A., "Understanding Hydrogen in Zirconium."

[5] S. Yamanaka, D. Setoyama, H. Muta, M. Uno, M. Kuroda, K. Takeda, and T. Matsuda, "Characteristics of zirconium hydrogen solid solution," *J. Alloys Compd.*, vol. 372, no. 1–2, pp. 129–135, Jun. 2004.

[6] K. Sadian, R. Johansson, and C. Alex, "Consequences of Hydrogen Pick-up in Fuel Cladding," 25-2010. http://es.scribd.com/doc/97923434/Consequences-of-Hydrogen-Pick-up-in-Fuel-Cladding. -Feb-2014].

[7] Elizabeth Jones, "Improved Digital Image Correlation (DIC) - File Exchange - MATLAB Central.". http://www.mathworks.com/matlabcentral/fileexchange/43073-improved-digital-image-correlation--dic-.

[8] IPCC, "Annex II: Special Report on Renewable Energy Sources and Climate Change Mitigation." 2011.